



Formation of Zn–Ca phyllomanganate nanoparticles in grass roots

B. Lanson, Matthew A. Marcus, S. Fakra, Frédéric Panfili, Nicolas Geoffroy, Alain Manceau

► To cite this version:

B. Lanson, Matthew A. Marcus, S. Fakra, Frédéric Panfili, Nicolas Geoffroy, et al.. Formation of Zn–Ca phyllomanganate nanoparticles in grass roots. *Geochimica et Cosmochimica Acta*, Elsevier, 2008, 72 (10), pp.2478 à 2490. <10.1016/j.gca.2008.02.022>. <insu-00334521>

HAL Id: insu-00334521

<https://hal-insu.archives-ouvertes.fr/insu-00334521>

Submitted on 13 Jan 2009

HAL is a multi-disciplinary open access archive for the deposit and dissemination of scientific research documents, whether they are published or not. The documents may come from teaching and research institutions in France or abroad, or from public or private research centers.

L'archive ouverte pluridisciplinaire **HAL**, est destinée au dépôt et à la diffusion de documents scientifiques de niveau recherche, publiés ou non, émanant des établissements d'enseignement et de recherche français ou étrangers, des laboratoires publics ou privés.

1 **Formation of Zn-Ca Phyllomanganate Nanoparticles in Grass Roots**

2
3 **Bruno Lanson^a, Matthew A. Marcus^b, Sirine Fakra^b, Frédéric Panfili^a,**

4 **Nicolas Geoffroy^a, Alain Manceau^a**

5
6 ^a Mineralogy & Environments Group, Maison des GéoSciences, Université Joseph Fourier –
7 CNRS, F-38041 Grenoble Cedex 9, France.

8 ^b Advanced Light Source, Lawrence Berkeley National Laboratory, Berkeley, California
9 94720, USA

10
11 * Corresponding author: [Bruno.Lanson@obs.ujf-grenoble.fr](mailto: Bruno.Lanson@obs.ujf-grenoble.fr)

12
13 Running title: Zn-Ca Phyllomanganate Nanoparticles in Grass Roots

14 **Abstract.** It is now well established that a number of terrestrial and aquatic
15 microorganisms have the capacity to oxidize and precipitate Mn as phyllomanganate.
16 However, this biomineralization has never been shown to occur in plant tissues, nor has the
17 structure of a natural Mn(IV) biooxide been characterized in detail. We show that the
18 graminaceous plant *Festuca rubra* (red fescue) produces a Zn-rich phyllomanganate with
19 constant Zn:Mn and Ca:Mn ratios (0.46 and 0.38, respectively) when grown on a
20 contaminated sediment. This new phase is so far the Zn-richest manganate known to form in
21 nature (chalcophanite has a Zn:Mn ratio of 0.33) and has no synthetic equivalent. Visual
22 examination of root fragments under a microscope shows black precipitates about ten to
23 several tens of microns in size, and their imaging with backscattered and secondary electrons
24 demonstrates that they are located in the root epidermis. In situ measurements by Mn and Zn
25 K-edge extended X-ray absorption fine structure (EXAFS) spectroscopy and X-ray diffraction
26 (XRD) with a micro-focused beam can be quantitatively described by a single-phase model
27 consisting of Mn(IV) octahedral layers with 22% vacant sites capped with tetrahedral and
28 octahedral Zn in proportions of 3:1. The layer charge deficit is also partly balanced by
29 interlayer Mn and Ca. Individual crystallites have a domain radius of 33 Å in the *ab* plane and
30 contain only 1.2 layers (~8.6 Å) on average. Since this biogenic Mn oxide consists mostly of
31 isolated layers, basal 00*l* reflections are essentially absent despite its lamellar structure.
32 Individual Mn layers are probably held together in the Mn-Zn precipitates by stabilizing
33 organic molecules. Zinc biomineralization by plants likely is a defense mechanism against
34 toxicity induced by excess concentrations of this metal in the rhizosphere.

1. INTRODUCTION

35
36
37 Graminaceous plants, like other so-called metal-tolerant plants, mostly sequester
38 metals in roots to protect reproductive and photosynthetic tissues (Li et al., 2000; Simon,
39 2005). The ability to store metals in underground tissues is used in phytoremediation to
40 reinstall a vegetation cover on heavily contaminated areas and limit the propagation of metals
41 into the food chain (Smith and Bradshaw, 1992; Cunningham et al., 1995; Vangronsveld et
42 al., 1995; Ma et al., 2003; Mench et al., 2003; Krämer, 2005). Panfili et al. (2005) showed that
43 the grass species *Festuca rubra* (red fescue) and *Agrostis tenuis* (colonial bentgrass)
44 accelerate the weathering of zinc sulfide when grown on contaminated dredged sediment, thus
45 increasing Zn bioavailability in the rhizosphere. After two years of plant growth, micrometer-
46 sized Mn-Zn black precipitates were observed at the surface of *Festuca rubra* roots, but not
47 characterized (Panfili, 2004). Zinc precipitation may be a bioactive tolerance mechanism in
48 response to metal toxicity, or a passive mineralization at the soil-root interface (Cotter-
49 Howells et al., 1999). Clarifying this issue and determining the mineralogy and structure of
50 this natural precipitate is important to enhance the effectiveness of using graminaceous plants
51 in phytoremediation. These questions are addressed here with electron microscopy and
52 synchrotron-based microanalytical tools, including X-ray fluorescence (μ -XRF), extended X-
53 ray absorption fine structure (μ -EXAFS) spectroscopy and X-ray diffraction (μ -XRD)
54 (Manceau et al., 2002b). Micro-XRD was employed to determine the nanocrystalline structure
55 of the Mn-Zn precipitates and the nature of defects (layer stacking faults, cationic vacancies
56 and occupancies, Mn, Zn, and Ca site configuration, stoichiometry) through modeling of their
57 scattering properties (Villalobos et al., 2006; Drits et al., 2007). We show that the root
58 precipitates are present in the root epidermis (the outermost layer of root cells) and consist of
59 a poorly crystallized phyllo-manganate with a constant Zn:Mn ratio higher than reported so far

60 for any natural and synthetic manganate. A structure model is proposed for this new
61 biomineral.

62

63

2. MATERIALS AND METHODS

64

65 2.1 Materials

66 The composition in major elements of the dredged sediment was 68.3 % SiO₂, 6.9 %
67 CaO, 4.8 % Al₂O₃, 2.4 % Fe₂O₃, 0.7 % P₂O₅, and 7.2% organic carbon, and the composition
68 in a trace metals was 4700 mg.kg⁻¹ Zn, 700 mg.kg⁻¹ Pb, and ~270 mg.kg⁻¹ Mn. Seeds of *F.*
69 *rubra* were sown in plastic pots filled with 40 kg of either the untreated sediment, the
70 sediment amended with 3 wt. % hydroxylapatite, or the sediment amended with 5 wt. %
71 Thomas basic slag. The pots were placed in a greenhouse without artificial lighting and daily
72 irrigated with tap water in an amount similar to the mean rainfall in northern France. After
73 two years of culture, the pots were dismantled to collect samples. The texture and color of the
74 sediment in areas colonized by the roots (upper 30 cm of the pots) were similar to a brown
75 silty soil, whereas the initial sediment was black and compact. Roots of *F. rubra* from the
76 treated and untreated pots were washed meticulously with distilled water to remove soil
77 particles from the surface and then freeze-dried.

78 The speciation of zinc in the initial sediment and in the rhizosphere of *F. rubra* after
79 the two years of vegetation was described previously (Panfili et al., 2005). Briefly, in the
80 untreated and unvegetated sediment, Zn was distributed as ~50% (mol ratio of total Zn)
81 sphalerite, ~40% Zn-ferrhydrite, and ~10 to 20% (Zn-Al)-hydrotalcite plus Zn-phyllsilicate.
82 In the presence of plants, ZnS was almost completely dissolved, and the released Zn bound to
83 phosphate (~40–60%) and to Zn phyllsilicate plus (Zn,Al)-hydrotalcite (~20–40%). The co-
84 addition of mineral amendment did not affect the Zn speciation in the vegetated sediment.

85

86 **2.2 Methods**

87 *2.2.1 Electron microscopy*

88 Regions of the roots rich in black precipitates were carbon-coated and examined in
89 secondary and backscattered electron modes by high-resolution scanning electron microscopy
90 (JEOL JSM-6320F with a field emission gun) and analyzed with energy dispersive X-ray
91 spectroscopy (EDS, Tracor analyzer).

92

93 *2.2.2 X-ray fluorescence, diffraction, and absorption spectroscopy*

94 The Zn:Mn and Ca:Mn ratios were measured with an Eagle III μ -XRF spectrometer
95 (Röntgenanalytik Messtechnik GmbH) equipped with a Rh anode and a 40 μ m poly-capillary.
96 The spectrometer was operated under vacuum at 20 kV and 400 μ A, and fluorescence was
97 measured for 300 s per point. Micro XRF, XRD and EXAFS data were collected on beamline
98 10.3.2 at the Advanced Light Source (ALS, Berkeley – Marcus et al., 2004a). Short root
99 fragments were attached to the tips of glass capillaries and cooled down to 110-150 K
100 (Oxford CryoSystems Cryo-Stream) to minimize radiation damage (Manceau et al., 2002b).
101 X-ray fluorescence maps were taken at 10 keV incident energy, with a beam size ranging
102 from 5 \times 5 μ m to 16 \times 7 μ m (H \times V). Fluorescence counts were collected for K, Ca, Mn, Fe and
103 Zn with a seven-element Ge solid-state detector and a counting time of 100 ms per pixel. For
104 μ -EXAFS measurements, the vertical beam size ranged from 5 to 7 μ m. A maximum of two
105 spectra per precipitate were taken at either the Mn or the Zn K-edge to prevent the reduction
106 of tetravalent to divalent Mn and the increase of structural disorder under the beam (Manceau
107 et al., 2002b). Diffraction data were collected with a CCD camera (Bruker SMART6000,
108 SMART software) at 17 keV ($\lambda = 0.729$ Å) and exposure times of 120-240 seconds. At this
109 energy, the incident flux and absorption cross-sections are low enough to make radiation
110 damage during an exposure negligible even at room temperature. A background pattern was

111 recorded next to each precipitate to subtract the scattering contribution from the root so as to
112 obtain the precipitate pattern. Diffraction patterns collected on different precipitates were all
113 statistically identical, and thus summed up to optimize data quality. Calibration of the energy
114 and camera distance were obtained using an Al₂O₃ standard and Fit2D software
115 (Hammersley, 1998). This software was also used to calculate the one-dimensional XRD
116 traces from the radial integration of the two-dimensional patterns.

117

118 2.2.3 Data processing

119 The EXAFS data were analyzed according to standard procedure (Teo, 1986; Marcus
120 et al., 2004b). The μ -XRD patterns were simulated following the trial-and-error approach
121 developed by Drits and Tchoubar (1990), and applied previously to natural and synthetic
122 phyllomanganates (Chukhrov et al., 1985; Manceau et al., 1997; Drits et al., 1998; Lanson et
123 al., 2000, 2002a, b; Gaillot et al., 2003, 2005, 2007; Villalobos et al., 2006). Details on the
124 program and fitting procedure can be found in the articles by Drits et al. (1998) and Plançon
125 (2002). The scattering background was considered to be linear in the 0.35-0.80 Å⁻¹ 1/d
126 interval (2.86-1.25 Å). The fit quality was evaluated over this interval using the conventional
127 R_{WP} and R_{Exp} values (Howard and Preston, 1989).

128

129 3. RESULTS AND INTERPRETATION

130

131 3.1 Optical and electron microscopy

132 Under the optical microscope, the Mn-Zn precipitates appear as black stains about
133 ten to several tens of micrometers in size on the root surface (Fig. 1a, EA-1). They are also
134 observed in backscattered electron microscopy (Fig. 1b) due to the presence of high-Z
135 elements (Mn, Zn, Ca, and minor Pb), but always are hardly noticeable in secondary electron

136 imaging mode (Fig. 1c). This suggests that the precipitates are engulfed in the root epidermis
137 (Cotter-Howells et al., 1999) and do not coat the root surface as iron and manganese plaques
138 do (Otte et al., 1989; St-Cyr and Campbell, 1996). No differences were observed among
139 precipitates from plants grown in the untreated and mineral amended sediments. This result,
140 together with the compartmentation of the precipitates inside the roots, suggests a biological
141 origin. This interpretation is supported also by the absence of Zn-rich phylломanganates in the
142 surrounding soil matrix (Panfili et al., 2005).

143

144 **3.2 Micro-XRF**

145 Elemental mapping of *F. rubra* roots shows that Zn is associated with Mn in
146 localized spots, and uniformly distributed without manganese in the vascular cylinder as
147 expected for this nutritive element (Fig. 2 – Rout and Das, 2003). All roots have Zn in their
148 central stele, but not all are speckled with Mn-Zn precipitates. Some root fragments are partly
149 covered by Zn-free Fe-rich plaques (Fig. EA-2). These plaques are made of ferric
150 oxyhydroxides, as indicated by their optical rusty color (Fig. 1a top right). In Zn-Mn-Ca
151 tricolor representation all Mn-Zn precipitates generally have the same color (Fig. 2), even
152 among different roots (Fig. EA-2), meaning that the relative proportions of Zn, Mn and Ca are
153 about the same. The correlation coefficient between Zn and Mn counts for the precipitates is
154 0.8, with P-value < 0.0001 for the Anova F-test (Fig. 2). The Zn:Mn atomic ratio was
155 calculated from the relative absorption jumps measured at the Mn and Zn K-edges on four
156 particles. For each particle, a pre-absorption edge background was removed first, and then a
157 linear fit to the post-edge region was extrapolated back to the edge to measure edge jumps.
158 The ratio of the Zn to Mn edge jumps is 0.310(7), which translates into a Zn:Mn ratio of
159 0.46(1) when taking into account the atomic absorptions of the two elements. A consistent
160 0.44 value was obtained independently with the Eagle III spectrometer. This analysis also

161 confirmed that root precipitates have a constant Ca:Mn ratio. An atomic ratio of 0.41 was
162 calculated after correction of the Ca-fluorescence from the root.

163

164 **3.3 Micro-EXAFS spectroscopy**

165 The Mn and Zn μ -EXAFS spectra for all precipitates were indistinguishable from
166 each other, and thus averaged to improve the signal-to-noise ratio. If the precipitates consisted
167 of an assemblage of distinct Zn and Mn species, the proportions of these species would most
168 likely vary among the analyzed grains, and this variability would be detected by μ -EXAFS
169 (Panfili et al., 2005). However, this was not the case, suggesting that all root precipitates
170 consist of a single species, hereafter referred to as "Mn-Zn precipitate", in agreement with μ -
171 XRF data.

172

173 *3.3.1 Mn-EXAFS in Mn-Zn precipitate*

174 Fig. 3 compares the EXAFS spectrum of Mn-Zn precipitate with those of reference
175 compounds. The references used are hollandite (Hol) and todorokite (Todo), two
176 tectomanganates with 2 \times 2 (Hol) and 3 \times 3 (Todo) tunnel structures, TcBi, a triclinic birnessite
177 with 31% Mn³⁺ in the layers, [Na⁺_{0.31}(H₂O)_{0.40}(Mn⁴⁺_{0.69}Mn³⁺_{0.31})O₂ – (Silvester et al., 1997;
178 Lanson et al., 2002a)], Lit, a synthetic lithiophorite [(Al_{0.67}Li_{0.32})(Mn⁴⁺_{0.68}Mn³⁺_{0.32})O₂(OH)₂ –
179 (Manceau et al., 2005)], HBi, a hexagonal birnessite prepared by equilibrating TcBi at pH 4
180 [H⁺_{0.33}Mn²⁺_{0.043}Mn³⁺_{0.123}(OH)⁻_{0.013}(Mn⁴⁺_{0.722}Mn³⁺_{0.111}Vac_{0.167})O₂ – (Silvester et al., 1997;
181 Lanson et al., 2000)], chalcophanite (Chalco), a Zn-rich phyllosilicate with one in seven
182 octahedral sites vacant and capped on each side of the surface layer by interlayer octahedral
183 Zn atoms [ZnMn₃O₇•3H₂O – (Wadsley, 1955)], and dBi, a turbostratic birnessite with no
184 interlayer Mn and no layer Mn³⁺ [Na⁺_{0.24}(H₂O)_{0.72}(Mn⁴⁺_{0.94}Vac_{0.06})O₂ – (Villalobos et al.,

185 2006)]. TcBi and Lit have a similar content of layer Mn^{3+} , but different Mn^{4+} - Mn^{3+} cation
186 ordering (Drits et al., 1997; Manceau et al., 2005).

187 Mn-Zn precipitate is not a tectomanganate because i) the second EXAFS oscillation
188 of tectomanganates is split or has a shoulder at 6.5 \AA^{-1} , depending on the tunnel size
189 (Manceau and Combes, 1988; Mckeown and Post, 2001; Manceau et al., 2007b), and ii) their
190 $[7.3\text{-}9.5 \text{ \AA}^{-1}]$ indicator region (Marcus et al., 2004b) does not match the data (Figs. 3a-b). In
191 the indicator region, Mn-Zn precipitate has a single maximum at $8.0\text{-}8.1 \text{ \AA}^{-1}$ like dBi, HBi,
192 and Chalco. The shape and position of this maximum is diagnostic of Mn^{4+} -rich manganate
193 layers with hexagonal symmetry (Gaillot et al., 2007). For example, this maximum is shifted
194 to 7.9 \AA^{-1} (i.e., consistent with longer distances) in Lit (Manceau et al., 2004) due to the large
195 amount of Mn^{3+} in the hexagonal layer. TcBi has a distinctive double peak with a minimum at
196 $7.9\text{-}8.0 \text{ \AA}^{-1}$ as a result of the split of the Mn-Mn distances induced by the linear ordering of
197 Mn^{3+} and Mn^{4+} cations in the layer (Drits et al., 1997; Lanson et al., 2002a; Gaillot et al.,
198 2003, 2007; Manceau et al., 2005). This cation ordering lowers the layer symmetry from
199 hexagonal to orthogonal. Thus, the Mn-Zn precipitate is a phyllomanganate having hexagonal
200 layer symmetry and little layer Mn^{3+} . The subtle differences between Mn-Zn precipitate and
201 some phyllomanganate references are more obvious when the data are Fourier transformed
202 (FT, Fig. 4). The phase of the $\text{Mn}1_{\text{E}}$ peak matches those of dBi, Chalco, and HBi, and is
203 shifted to a shorter distance relative to Lit. In phyllomanganates, the $\text{Mn}1_{\text{E}}$ peak represents
204 Mn atoms in the first-neighbor layer octahedra (Manceau and Combes, 1988). Therefore, its
205 phase depends on the nearest Mn-Mn distance (Mn-Mn1 pair), and is sensitive to the amount
206 of Mn^{3+} in the layer similarly to the phase of the O peak. However, the sensitivity of the phase
207 of this peak to the presence of Mn^{3+} is not high enough to distinguish HBi (11% layer Mn^{3+}
208 per octahedral site) from dBi and Chalco (0% – Fig. EA-3). The $\text{Mn}3_{\text{E}}$ peak is twice as
209 sensitive as the $\text{Mn}1_{\text{E}}$ peak because it arises from the third-neighbor octahedra at twice the

210 Mn-Mn1 distance (see for example Fig. 11 in Manceau et al., 2005). The sensitivity is now
211 high enough to differentiate HBi from dBi and Chalco, as shown in Fig. 4. Thus, using the
212 phase of the Mn1_E and Mn3_E peaks as chemical probes to the layer composition, we conclude
213 that Mn-Zn precipitate has less Mn³⁺ in the octahedral layers than HBi (11%), if any.
214 Confirming evidence is found in the comparison of the frequency of EXAFS spectra. Fig. 3
215 shows that the overall EXAFS frequency, and hence interatomic distances, increase from
216 dBi/Chalco/Mn-Zn precipitate, to HBi, to Lit/TcBi, as a result of the increasing amount of
217 layer Mn³⁺ (Gaillot et al., 2007).

218 In contrast to the Mn1 peak, the phase of the O peak (i.e., average Mn-O distance in
219 the layer and interlayer) matches those of the two Mn³⁺-free references (dBi, Chalco) and is
220 slightly shifted to lower distance relative to both HBi and Lit. This shift is barely visible in
221 Fig. 4, but clearly apparent when the [1-3 Å] $R+\Delta R$ interval is expanded (Fig. EA-3). Thus,
222 Mn-Zn precipitate has no detectable Mn³⁺ in the layer similarly to dBi and Chalco, nor in the
223 interlayer, in contrast to HBi.

224 The FT of Mn-Zn precipitate also differs from that of HBi by the absence of the
225 Mn1_{TC} peak from Mn_{layer}-Me pairs at ~ 3.5 Å ($R + \Delta R \sim 3.1$ Å), where Me is an interlayer
226 metal cation, such as Mn, Zn, or Pb, in triple-corner sharing position above or below vacant
227 layer sites (TC linkage – Manceau et al., 2002a). When there are interlayer Mn atoms, this
228 peak is intense because each interlayer Mn is surrounded by as many as six Mn_{layer} neighbors.
229 In contrast, Mn_{layer} atoms near an octahedral vacancy have fewer interlayer Mn neighbors,
230 their exact number depending on the density of layer vacancies and composition of the
231 interlayer. Here, the lack of Mn1_{TC} peak in Mn-Zn precipitate suggests that it has no
232 detectable Me cations on either side of the layer vacancies. The Mn5_E peak is also absent in
233 the FT of Mn-Zn precipitate, as in dBi, but not HBi nor Chalco. This peak arises from the 5th
234 Mn shell at about $2.90 \times 3 = 8.7$ Å, and is enhanced by forward scattering from two

235 intervening Mn_{layer} (Manceau et al., 2005). The absence of this peak in Mn-Zn precipitate
236 indicates that the octahedral layers have a small lateral dimension. This peak is also absent in
237 Lit, but in this case because the Mn-Mn5 shell is split as a result of the Mn^{4+} - Mn^{3+} ordering in
238 the layer (Manceau et al., 2005).

239

240 3.3.2 Zn-EXAFS in Mn-Zn precipitate

241 The best spectral match of Mn-Zn precipitate to our Zn species database was
242 obtained with tetrahedrally coordinated Zn ($^{\text{IV}}\text{Zn}$) sorbed above/below octahedral vacancies of
243 a phyllosulfate ($^{\text{IV}}\text{TC}$ site – Fig. 5a). This Zn complex is common in nature and its local
244 structure has been described previously (Manceau et al., 2000b, 2002a; Marcus et al., 2004b;
245 Isaure et al., 2005; Toner et al., 2006). Although the $^{\text{IV}}\text{Zn}$ -sorbed phyllosulfate reference
246 provides a good approximation of Zn local structure in Mn-Zn precipitate, there are
247 significant differences between the two spectra, particularly in the phase mismatches between
248 6.5 and 10 \AA^{-1} , and the symmetry of the first and second oscillations. These differences have
249 been documented previously and result from the mixed occupancy of the TC site by
250 tetrahedral and octahedral Zn (Manceau et al., 2002a, 2007b). Adding the chalcophanite or
251 $^{\text{VI/IV}}\text{Zn}$ -sorbed dBi reference (Fig. 5b – Toner et al., 2005a, 2006) in a two-component linear
252 fit to the data compensated for the phase shift and asymmetry of the first oscillation, but not
253 entirely for that of the second (Fig. 5c). All attempts to suppress this residual by adding a
254 third component to the linear fit failed. Therefore, although there is some uncertainty on the
255 exact configuration of the minor $^{\text{VI}}\text{Zn}$ site, the $^{\text{IV}}\text{TC} + ^{\text{VI}}\text{TC}$ model is the best description of
256 the data we can offer. Consideration of an edge-sharing complex ($^{\text{VI}}\text{TE}$) at layer edges did not
257 reproduce the phase as well as the $^{\text{VI}}\text{TC}$ surface species. The $^{\text{VI}}\text{TC}$ species may occur also at
258 the edge of the Mn-Zn precipitate layer, instead of the basal surface, in which case it has a
259 slightly different binding environment from that of dBi. Thus, the dBi and chalcophanite

260 standards may not be the best proxies for the ^{VI}TC species. The fraction of each Zn species
261 derived from the two-component least-squares fit is $87 \pm 10\%$ ^{IV}TC and $27 \pm 10\%$ ^{VI}TC .

262

263 3.3.3 Zn-EXAFS in Zn-only precipitate

264 A few spots in the μ -XRF maps contained Zn and little else detectable. EXAFS
265 spectroscopy identified zincite (ZnO) and sphalerite (ZnS), two mineral species originally
266 present in the untreated sediment (Isaure et al., 2002). These grains are likely residual slag
267 material stuck to the root surface that were not removed by washing. None of the Zn species
268 formed in the rhizosphere of *F. rubra* after the two years of experiment were detected in or at
269 the root surface.

270

271 3.3.4 Zn-EXAFS in the root vascular cylinder

272 Micro-EXAFS spectra were recorded in the vascular cylinder of four distinct roots, at
273 spots containing little Mn. All spectra were indistinguishable, indicating that Zn speciation is
274 uniform, and thus averaged. The resulting Root spectrum has the same frequency as the Mn-
275 Zn precipitate spectrum, which suggests that Zn is also mostly tetrahedral in the roots (Fig.
276 5d). However, in contrast to Mn-Zn precipitate, the second and third oscillations of the Root
277 spectrum are not split, indicative of “light” backscatters from second-shell contributions.
278 Consistently, the best spectral match to our organic and inorganic database of the Root
279 spectrum was provided with Zn in a biofilm (Zncell7, Fig. 5e). This reference has $80 \pm 10\%$
280 Zn complexed to phosphoryl groups and $20 \pm 10\%$ to carboxyl groups (Toner et al., 2005b).
281 Consistent with this other study, consideration of carboxyl (citrate, Fig. 5f) and phosphate
282 (phytate, Fig. 5g; Zn-sorbed *Penicillium chrysogenum*, Fig. 5h – Sarret et al., 1998a) ligands
283 alone, did not yield an optimal fit to the data. Zinc preferential binding to phosphate groups
284 has been reported also in the roots of *Arabidopsis halleri* and *A. lyrata* grown hydroponically,

285 on bacterial and fungi cells, and in biofilms (Sarret et al., 1998b, 2002; Fein et al., 2001).
286 These studies have shown that Zn has a higher affinity for phosphate than for carboxyl
287 groups, which is consistent with the predominance of the phosphate species in *F. rubra* roots.

288

289 **3.4 Micro-XRD**

290 *3.4.1 Qualitative description of the data*

291 According to μ -XRF and μ -EXAFS, Mn-Zn precipitate is a phyllo-manganate with
292 hexagonal layer symmetry, little to no layer Mn^{3+} , less interlayer Mn^{3+} than HBi, and as much
293 as 0.46 interlayer Zn per total Mn, of which $87 \pm 10\%$ is tetrahedral and $27 \pm 10\%$ octahedral.
294 Despite its lamellar structure, the XRD pattern of Mn-Zn precipitate shows no patent basal
295 reflections (Fig. 6). The XRD trace is dominated by two reflections at ~ 2.45 and ~ 1.42 Å, the
296 first one being asymmetric towards higher $1/d$ values. This profile is characteristic of lamellar
297 compounds with turbostratic stacking, i.e., lacking well-defined displacement/rotation
298 between successive layers (Warren, 1941; Biscoe and Warren, 1942; Brindley, 1980). The
299 positions, profiles, and relative intensities of the two peaks match the [20,11] and [02,31]
300 scattering bands of turbostratic birnessite, choosing a C-centered cell for their crystallographic
301 assignment (Drits et al., 1997, 2007; Villalobos et al., 2006). Their d -spacings are in the ratio
302 of 1.73, close to the $\sqrt{3}$ value for hexagonal symmetry. Their profiles are controlled by the
303 structure factor and can thus be used for structural determinations (Villalobos et al., 2006;
304 Drits et al., 2007), as shown below.

305

306 *3.4.2 Simulation of the 0.35-0.80 Å⁻¹ 1/d interval*

307 XRD simulations were performed with the C-centered unit-cell parameters $b =$
308 2.850 Å, $a = b\sqrt{3} = 4.936$ Å, $\gamma = 90^\circ$ derived from the position of the [20,11] and [02,31]
309 bands, $d_{(001)} = 7.20$ Å, and a random layer stacking ($W_r = 100\%$, Fig. EA-4). The atomic

310 coordinates for the ^{IV}TC and ^{VI}TC sites were considered to be the same as those in Zn-sorbed
311 birnessite (Table 1 – Lanson et al., 2002b). The Ca position was assumed to be close to that in
312 Ca-rich birnessite (Drits et al., 1998), that is in the mid-plane of the interlayer almost above a
313 tetrahedral surface site (TE position – Fig. EA-5). Thus, parameters optimized in the
314 simulations are the amount of vacant layer sites, the amount, position, and coordination of
315 interlayer Zn²⁺ and Mn^{2+,3+}, the *xy* coordinates of Ca²⁺, the position of water molecules, and
316 the size of the coherent scattering domains (CSDs) in the *ab* plane. The CSDs were
317 considered to have a disk-like shape, whose average radius was constrained by fitting the
318 maximum at ~2.45 Å (Villalobos et al., 2006).

319 Since the phyllosilicate has 0.46 interlayer Zn per total Mn, at least 0.186 vacant
320 layer sites per octahedron are needed to accommodate all Zn [(0.186 × 2) / (1.00 - 0.186) =
321 0.46]. In this case, every vacant site is capped by one Zn on either side. No satisfactory
322 agreement between theory and experiment could be obtained with this model, regardless of
323 the amount and position of Ca²⁺. In particular, the high *1/d* tail of the [20,11] band at ~0.43-
324 0.45 Å⁻¹ was poorly reproduced (Fig. 7a – R_{WP} = 3.57%; R_{Exp} = 1.57%). To reproduce this
325 feature it was necessary to increase the density of vacant sites to 0.22, and thus to introduce
326 interlayer Mn in TC and TE sites to keep the Zn:Mn ratio constant. Our best theoretical model
327 to the data is shown in Fig. 7b (R_{WP} = 3.49%; R_{Exp} = 1.57%), and structural parameters are
328 listed in Tables 1 and 2. The structural formula is
329 [(Mn_{0.78}Vac_{0.22})O₂]^{TC}Mn_{0.010}^{TE}Mn_{0.046}^{VI}Zn_{0.088}^{IV}Zn_{0.300}Ca_{0.318}(H₂O)_{0.972}], and the structure
330 model is schematized in Figs. 8 and EA-5. The refined model contains 0.38 Ca per Mn, in
331 agreement with μ-XRF data (0.41), at a position [(-0.410, 0, ½) and symmetric positions]
332 slightly shifted from the ideal TE position [(-0.333, 0, ½) – Fig. EA-5]. Interlayer H₂O
333 molecules that are not bound to Zn and interlayer Mn are located in (0.220, 0, ½) and
334 symmetric positions. This position is similar to ordered (Lanson et al., 2002a) and disordered

335 (Villalobos et al., 2006) Na-exchanged birnessite varieties. It allows for the formation of
336 strong H-bonds with O_{layer} atoms [$d(O_{\text{layer}}-H_2O_{\text{inter.}}) = 2.66 \text{ \AA}$, Table 2]. Overall, only the Mn
337 TE position is new, all others have been described previously for other birnessite varieties.

338

339 *3.4.3 Sensitivity of calculated XRD patterns to structural parameters*

340 As the optimal fit to data was obtained using a trial-and-error approach, the
341 sensitivity of the XRD simulations to key structural parameters needs to be assessed. A key
342 parameter for birnessite's ability to sorb trace metals is the origin of the layer charge. In the
343 present model, the layer charge arises from layer vacancies only, not at all from substitution
344 of Mn^{3+} for Mn^{4+} in the layer, because the hexagonal layer symmetry and small b unit-cell
345 dimension (2.85 \AA) are incompatible with appreciable amount of Mn^{3+} in the layer (Gaillot et
346 al., 2005, 2007; Manceau et al., 2005). When birnessite contains $\sim 25\%$ layer Mn^{3+} per
347 octahedral site with the long Mn-O bonds oriented at random, $b = 2.895 \text{ \AA}$ (Gaillot et al.,
348 2007) and the [20,11] and [02,31] bands are shifted to lower $1/d$ values relative to data ($R_{\text{WP}} =$
349 7.15% ; Fig. 7c). Mn-Zn precipitate has the same b value as HBi (2.850 \AA) which contains
350 11% layer Mn^{3+} per octahedral site (Lanson et al., 2000). Based on EXAFS results, this
351 amount is regarded as an upper limit. Also, if the layer contained a high proportion of Mn^{3+}
352 cations ordered in rows, as in triclinic birnessite, a similar b value ($2.84\text{-}2.85 \text{ \AA}$) would be
353 measured but the [02,31] band would be a doublet due to the departure from hexagonal
354 symmetry (Drits et al., 2007; Gaillot et al., 2007). Calculations show that the band splitting
355 decreases with the layer dimension, but that it should still be observed for a CSD dimension
356 of 33 \AA , the optimal CSD value (Fig. 7d – $R_{\text{WP}} = 6.79\%$).

357 The sensitivity of XRD profiles to the amount, coordination, and position of high-Z
358 interlayer scatterers, and to the number of vacant layer sites is illustrated next. If interlayer
359 Mn atoms are located only in $^{\text{VI}}\text{TC}$ sites (0.056 per octahedron) rather than distributed over

360 ^{VI}TE and ^{VI}TC sites (0.046 and 0.010, respectively), the dip at $\sim 0.52 \text{ \AA}^{-1}$ is deeper and the
361 intensity of the broad hump at $\sim 0.60 \text{ \AA}^{-1}$ is increased (Fig. 7e – $R_{WP} = 3.60\%$). When the
362 number of interlayer Ca^{2+} is decreased from 0.318 to 0.240, there is a deficit of intensity in
363 the $0.43\text{-}0.45 \text{ \AA}^{-1}$ region (Fig. 7f – $R_{WP} = 3.54\%$). Similarly, decreasing the number of
364 interlayer Zn from 0.388 to 0.244, and that of vacant layer sites from 0.22 to 0.15 broadens
365 the high $1/d$ tail of the [20,11] band and shifts the hump at $\sim 0.60 \text{ \AA}^{-1}$ to lower $1/d$ values (Fig.
366 7g – $R_{WP} = 4.92\%$). Increasing the proportion of octahedrally coordinated interlayer Zn from
367 23% to 50% also broadens the high $1/d$ tail of the [20,11] band and increases the intensity of
368 the broad hump at $\sim 0.60 \text{ \AA}^{-1}$ (Fig. 7h – $R_{WP} = 3.99\%$). Finally, the sensitivity of XRD profiles
369 to ^{IV}Zn , ^{VI}Zn , and Ca coordinates is shown in Figure EA-6.

370

371 *3.4.4 Simulation of the $0.05\text{-}0.35 \text{ \AA}^{-1}$ $1/d$ interval*

372 Despite the lamellar structure of Mn-Zn precipitate, its XRD pattern lacks well-
373 defined $00l$ reflections. To assess the possible origin of this oddity, the 001 and 002
374 reflections were calculated for crystallites with extremely small CSD dimension along the c^*
375 axis (Fig. 9). Calculations show that at least two layers are required to modulate the scattering
376 profile at low $1/d$ values, otherwise the X-ray intensity steadily decreases with increasing $1/d$
377 (Fig. 9). The best fit to data was obtained with a mixture of crystallites containing 1, 2, and 3
378 layers in the ratio of 20:3:1, respectively, leading to an average CSD dimension along the c^*
379 axis of 1.2 layers ($\sim 8.6 \text{ \AA}$).

380

381 **4. DISCUSSION**

382

383 **4.1 Structure model**

384

385 *4.1.1 Amount of vacant sites and Zn loading*

386 Except for one sample obtained by metal sorption on poorly crystalline Mn oxides
387 (Nelson et al., 1999), the new Zn-rich phyllosulfate contains higher amounts of vacant
388 layer sites (0.22 per layer octahedron) and transition elements (0.44 total Mn and Zn per layer
389 octahedron) than any other natural and synthetic variety described so far (0.167 and 0.22,
390 respectively; Lanson et al., 2000, 2002b; Villalobos et al., 2006). The constant Zn:Mn ratio of
391 Mn-Zn precipitate suggests that Zn co-precipitated with Mn by a yet unknown mechanism to
392 form a chemically well-defined phase as natural solids formed by metal sorption on pre-
393 existing mineral surfaces are chemically heterogeneous (see for example Manceau et al.,
394 2007b).

395

396 *4.1.2 Presence of heavy scatterers above and below vacant layers sites*

397 According to XRD and Zn-EXAFS, Mn-Zn precipitate has 0.300 ^{IV}Zn and 0.088
398 ^{VI}Zn per octahedron in TC position (Table 1). The Zn-Mn pairs are detected at the Zn K-edge
399 (Fig. EA-7) but not at the Mn K-edge for two possible reasons. In a vacancy-free layer, each
400 Mn has six nearest-neighbor Mn atoms. In Mn-Zn precipitate, this number is 4.25 if two
401 vacancies cannot be adjacent which is always the case in layered structures (Manceau et al.,
402 2000a). Thus, each Mn octahedron is surrounded statistically by 1.75 vacant sites. With 80%
403 of these vacant sites capped by Me cations on both sides, and 20% on one side only, Mn_{layer}
404 atoms are coordinated on average to $1.75 \times (0.2 + (0.8 \times 2)) = 3.15$ Me in TC sites. This
405 number is about half the value for Zn, as each Zn is linked to six Mn_{layer}. Structural disorder
406 also can be invoked to explain the absence of Mn-Zn pairs in Mn-EXAFS. The TC position is
407 occupied by at least three types of complex: 0.300 ^{IV}Zn, 0.088 ^{VI}Zn, and 0.010 ^{VI}Mn, and the
408 TE position by 0.046 Mn. Each Mn_{layer}^(TC,TE)Me pair has a different distance, and this broad
409 distribution results in an apparent loss of coordination.

410

411 **4.2 Intensity of basal reflections**

412 Birnessite and vernadite minerals were given different names because the basal
413 reflections of birnessite at 7.2-7.0 Å (001) and 3.6-3.5 Å (002) were not observed originally in
414 the diffraction pattern of vernadite (Chukhrov and Gorshkov, 1980; Chukhrov et al., 1980).
415 However, recent studies have shown that natural vernadite and its biogenic and chemical (δ -
416 MnO₂) analogs most often display a 001 reflection when their XRD pattern is recorded on
417 modern diffractometers (Mandernack et al., 1995; Villalobos et al., 2003, 2005; Jurgensen et
418 al., 2004; Webb et al., 2005b; Bodeř et al., 2007; Manceau et al., 2007a, b), thus confirming
419 the view of Arrhenius et al. (1978) and Giovanoli (1980) that this mineral is a *c*-disordered
420 variety of birnessite. Villalobos et al. (2006) showed that basal reflections are present when
421 the diffracting crystallites have only 2-3 layers, on average. Here, this number is as low as 1.2
422 layers, meaning that Mn-Zn precipitate is essentially an assemblage of isolated layers.
423 Measurements of the Mn edge jumps on different Mn-Zn precipitates provide an inkling of
424 how the constitutive nanoparticles are joined at particle or so-called grain boundaries. The Mn
425 edge jump was typically between 0.2 and 0.3 for aggregates ~15-25 μ m in diameter, which
426 indicates that the phylломanganate represents only a small fraction (~20 volume %) of the
427 black precipitates, thus revealing a high micro-porosity. This porosity is possibly filled, at
428 least partly, by organics that may help disrupt the parallelism of the layers, but also to tie
429 them together.

430

431 **4.3 Biologically induced oxidation of manganese**

432 Many microorganisms have the capacity to oxidize and precipitate Mn as manganate
433 (Tebo et al., 2004, and references therein). Since biological oxidation of Mn is generally
434 faster than abiotic oxidation, most natural Mn oxides are considered to be biogenic.

435 *Pseudomonas putida* (Villalobos et al., 2003, 2006; Toner et al., 2005a), *Leptothrix*
436 *discophora* (Nelson et al., 1999, 2002; Nelson and Lion, 2003; Jurgensen et al., 2004;
437 Saratovsky et al., 2006), and *Bacillus* sp. strain SG-1 (Mandernack et al., 1995; Tebo et al.,
438 1998; Webb et al., 2005a, b) are the three fairly-well characterized bacterial model systems
439 for the oxidation of manganese in the environment. Manganese oxidation and the subsequent
440 precipitation of Mn(III,IV) bioxides by microscopic fungi is also well documented (Krumbein
441 and Jens, 1981; Emerson et al., 1989; Schulze et al., 1995; Tani et al., 2003, 2004; Miyata et
442 al., 2004, 2006a, b; Thompson et al., 2005). Here, we showed that Mn can be biomineralized
443 also in higher living organisms, such as plants. Except for its atypical high Zn content and the
444 structural consequences thereof, this new manganese biomineral is no exception to the
445 intrinsic nanocrystalline nature of biogenic phyllomanganates.

446 Although the mechanism of Mn(II) to Mn(IV) oxidation is presently unknown, the
447 constant Zn:Mn ratio of the new Mn biooxide suggests the existence of a well-defined
448 bioactive process, likely in response to metal toxicity. The occurrence of Zn-Mn precipitate
449 only in the root epidermis and the absence in the roots of any Zn-rich species from the soil
450 matrix (Panfili et al., 2005) suggest that Mn oxidation did not occur in the rhizosphere, and
451 thus does not result from bacterial activity or abiotic reaction. Divalent manganese may have
452 been complexed and transported to the roots by phytosiderophores (Römheld, 1991), and then
453 oxidized by the plant itself or by endomycorrhizal fungi, as shown for wheat and soybean
454 (Schulze et al., 1995; Thompson et al., 2005, 2006).

455 Knowing how to stimulate the formation of this new phase in biological systems, or
456 how to synthesize it abiotically, would be a significant progress towards Zn immobilization in
457 contaminated environments and their (phyto-)remediation. Formation of this new phase could
458 in particular facilitate the growth of plants in highly contaminated environments in lowering
459 the concentration of bio-available Zn in the rhizosphere.

460

461

ACKNOWLEDGMENTS

462

463

464

465

466

467

468

469

470

471

472

The following persons are thanked for their contribution on various aspects of this work: Fabienne Marseille and Bertrand Girondelot (CNRSSP, Douai) for the setup of pot experiments, Clément Falk (LGIT, Grenoble) for optical microscopy on Mn-Zn precipitate, Serge Nitsche, Damien Chaudanson, and Alain Baronnet (CRMCN, Marseilles) for SEM analysis, Manuel Muñoz (LGCA, Grenoble) for XRF measurements on the Eagle spectrometer, Didier Arnal, Nicole Paoletti, and Gérard Souche (R&S, Montpellier) for growing *Festuca rubra* in hydroponic conditions, and Benoît Jaillard and Philippe Hinsinger (R&S, Montpellier) for fruitful discussions about metal uptake by plants. This research was supported by the ACI/FNS Ecco (EcoDyn) program. The ALS is supported by the Director, Office of Energy Research, Office of Basic Energy Sciences, Materials Sciences Division of the U.S. Department of Energy, under Contract No. DE-AC02-05CH11231.

473
474
475
476
477
478
479
480
481
482
483
484
485
486
487
488
489
490
491
492
493
494
495
496

REFERENCES

- Arrhenius G., Cheung K., Crane S., Fisk M., Frazer J., Korkisch J., Melin T., Nakao S., Tsai A., and Wolf G. (1978) Counterions in marine manganates. In *La genèse des nodules de manganèse* (ed. C. Lalou). Proc. Int. Coll. CNRS **289**, 333-356.
- Biscoe J. and Warren B.E. (1942) An X-ray study of carbon black. *J. App. Phys.* **13**, 364-371.
- Bodeř S., Manceau A., Geoffroy N., Baronnet A., and Buatier M. (2007) Formation of todorokite from vernadite in Ni-rich hemipelagic sediments. *Geochim. Cosmochim. Acta* **71**, in press.
- Brese N.E. and O' Keeffe M. (1991) Bond-valence parameters for solids. *Acta Crystallogr.* **B47**, 192-197.
- Brindley G.W. (1980) Order-disorder in clay mineral structures. In *Crystal Structures of Clay Minerals and their X-ray Identification* (ed. G.W. Brindley and G. Brown), pp. 125-195. Mineralogical Society.
- Chukhrov F.V. and Gorshkov A.I. (1980) Reply to R. Giovanoli's comment. *Miner. Depos.* **15**, 255-257.
- Chukhrov F.V., Gorshkov A.I., Rudnitskaya E.S., Berezovskaya V.V., and Sivtsov A.V. (1980) Manganese minerals in clays: A review. *Clays & Clay Miner.* **28**, 346-354.
- Chukhrov F.V., Sakharov B.A., Gorshkov A.I., Drits V.A., and Dikov Y.P. (1985) Crystal structure of birnessite from the Pacific ocean. *Int. Geol. Rev.* **27**, 1082-1088.
- Cotter-Howells J.D., Champness P.E., and Charnock J.M. (1999) Mineralogy of Pb-P grains in the roots of *Agrostis capillaris* L. by ATEM and EXAFS. *Miner. Mag.* **63**, 777-789.
- Cunningham S.D., Berti W.R., and Huang J.W. (1995) Phytoremediation of contaminated soils. *Trends Biotech.* **13**, 393-397.

- 497 Drits V.A. and Tchoubar C. (1990) *X-ray diffraction by disordered lamellar structures:*
498 *Theory and applications to microdivided silicates and carbons.* Springer-Verlag.
- 499 Drits V.A., Silvester E.J., Gorshkov A.I., and Manceau A. (1997) The structure of monoclinic
500 Na-rich birnessite and hexagonal birnessite. Part 1. Results from X-ray diffraction and
501 selected area electron diffraction. *Amer. Mineral.* **82**, 946-961.
- 502 Drits V.A., Lanson B., Gorshkov A.I., and Manceau A. (1998) Substructure and
503 superstructure of four-layer Ca-exchanged birnessite. *Amer. Mineral.* **83**, 97-118.
- 504 Drits V.A., Lanson B., and Gaillot A.C. (2007) Birnessite polytype systematics and
505 identification by powder X-ray diffraction. *Amer. Mineral.* **92**, 771-788.
- 506 Emerson D., Garen R.E., and Ghiorse W.C. (1989) Formation of *Metallogenium*-like
507 structures by a manganese-oxidizing fungus. *Arch. Microbiol.* **151**, 223-231.
- 508 Fein J.B., Martin A.M., and Wightman P.G. (2001) Metal adsorption onto bacterial surfaces:
509 Development of a predictive approach. *Geochim. Cosmochim. Acta* **65**, 4267-4273.
- 510 Gaillot A.-C., Flot D., Drits V.A., Manceau A., Burghammer M., and Lanson B. (2003)
511 Structure of synthetic K-rich birnessite obtained by high-temperature decomposition
512 of KMnO_4 . I. Two-layer polytype from 800°C experiment. *Chem. Mater.* **15**, 4666-
513 4678.
- 514 Gaillot A.-C., Lanson B., and Drits V.A. (2005) Structure of birnessite obtained from
515 decomposition of permanganate under soft hydrothermal conditions. 1. Chemical and
516 structural evolution as a function of temperature. *Chem. Mater.* **17**, 2959-2975.
- 517 Gaillot A.-C., Drits V.A., Manceau A., and Lanson B. (2007) Structure of the synthetic K-rich
518 phyllomanganate birnessite obtained by high-temperature decomposition of KMnO_4 -
519 Substructures of K-rich birnessite from 1000°C experiment. *Micropor. Mesopor.*
520 *Mater.* **98**, 267-282.
- 521 Giovanoli R. (1980) Vernadite is random-stacked birnessite. *Mineral. Depos.* **15**, 251-253.

522 Hammersley A.P. (1998) FIT2D V9.129 - Reference manual V3.1, Vol. 346. ESRF internal
523 report - ESRF98HA01T.

524 Howard S.A. and Preston K.D. (1989) Profile fitting of powder diffraction patterns. In
525 *Modern Powder Diffraction*, Vol. 20 (ed. D.L. Bish and J.E. Post), pp. 217-275.
526 Mineralogical Society of America.

527 Isaure M.P., Laboudigue A., Manceau A., Sarret G., Tiffreau C., Trocellier P., Lamble G.,
528 Hazemann J.L., and Chateigner D. (2002) Quantitative Zn speciation in a
529 contaminated dredged sediment by μ -PIXE, μ -SXRF, EXAFS spectroscopy and
530 principal component analysis. *Geochim. Cosmochim. Acta* **66**, 1549-1567.

531 Isaure M.P., Manceau A., Geoffroy N., Laboudigue A., Tamura N., and Marcus M.A. (2005)
532 Zinc mobility and speciation in soil covered by contaminated dredged sediment using
533 micrometer-scale and bulk-averaging X-ray fluorescence, absorption and diffraction
534 techniques. *Geochim. Cosmochim. Acta* **69**, 1173-1198.

535 Jurgensen A., Widmeyer J.R., Gordon R.A., Bendell Young L.I., Moore M.M., and Crozier
536 E.D. (2004) The structure of the manganese oxide on the sheath of the bacterium
537 *Leptothrix discophora*: An XAFS study. *Amer. Mineral.* **89**, 1110-1118.

538 Krämer U. (2005) Phytoremediation: novel approaches to cleaning up polluted soils. *Curr.*
539 *Opin. Biotechnol.* **16**, 133-141.

540 Krumbein W.E. and Jens K. (1981) Biogenic rock varnishes of the Negev Desert (Israel) an
541 ecological study of iron and manganese transformation by cyanobacteria and fungi.
542 *Oecologia* **50**, 25-38.

543 Lanson B., Drits V.A., Silvester E.J., and Manceau A. (2000) Structure of H-exchanged
544 hexagonal birnessite and its mechanism of formation from Na-rich monoclinic
545 buserite at low pH. *Amer. Mineral.* **85**, 826-838.

546 Lanson B., Drits V.A., Feng Q., and Manceau A. (2002a) Structure of synthetic Na-birnessite:
547 Evidence for a triclinic one-layer unit cell. *Amer. Mineral.* **87**, 1662-1671.

548 Lanson B., Drits V.A., Gaillot A.-C., Silvester E., Plancon A., and Manceau A. (2002b)
549 Structure of heavy-metal sorbed birnessite: Part 1. Results from X-ray diffraction.
550 *Amer. Mineral.* **87**, 1631-1645.

551 Li Y.M., Chaney R.L., Siebielec G., and Kerschner B.A. (2000) Response of four turfgrass
552 cultivars to limestone and biosolids-compost amendment of a zinc and cadmium
553 contaminated soil at Palmerton, Pennsylvania. *J. Environ. Qual.* **29**, 1440-1447.

554 Ma M., Lau P.S., Jia Y.T., Tsang W.K., Lam S.K.S., Tam N.F.Y., and Wong Y.S. (2003) The
555 isolation and characterization of Type 1 metallothionein (MT) cDNA from a heavy-
556 metal-tolerant plant, *Festuca rubra* cv. Merlin. *Plant Sci.* **164**, 51-60.

557 Manceau A. and Combes J.-M. (1988) Structure of Mn and Fe oxides and hydroxides: A
558 topological approach by EXAFS. *Phys. Chem. Miner.* **15**, 283-295.

559 Manceau A., Drits V.A., Silvester E.J., Bartoli C., and Lanson B. (1997) Structural
560 mechanism of Co²⁺ oxidation by the phylломanganate buserite. *Amer. Mineral.* **82**,
561 1150-1175.

562 Manceau A., Lanson B., Drits V.A., Chateigner D., Gates W.P., Wu J., Huo D., and Stucki
563 J.W. (2000a) Oxidation-reduction mechanism of iron in dioctahedral smectites: I.
564 Crystal chemistry of oxidized reference nontronites. *Amer. Mineral.* **85**, 133-152.

565 Manceau A., Lanson B., Schlegel M.L., Harge J.-C., Musso M., Eybert Berard L., Hazemann
566 J.L., Chateigner D., and Lambie G.M. (2000b) Quantitative Zn speciation in smelter-
567 contaminated soils by EXAFS spectroscopy. *Amer. J. Sci.* **300**, 289-343.

568 Manceau A., Lanson B., and Drits V.A. (2002a) Structure of heavy metal sorbed birnessite.
569 Part III: Results from powder and polarized extended X-ray absorption fine structure
570 spectroscopy. *Geochim. Cosmochim. Acta* **66**, 2639-2663.

571 Manceau A., Marcus M.A., and Tamura N. (2002b) Quantitative speciation of heavy metals
572 in soils and sediments by synchrotron X-ray techniques. In *Applications of*
573 *Synchrotron Radiation in Low-Temperature Geochemistry and Environmental*
574 *Sciences*, Vol. 49, pp. 341-428.

575 Manceau A., Marcus M.A., Tamura N., Proux O., Geoffroy N., and Lanson B. (2004) Natural
576 speciation of Zn at the micrometer scale in a clayey soil using X-ray fluorescence,
577 absorption, and diffraction. *Geochim. Cosmochim. Acta* **68**, 2467-2483.

578 Manceau A., Tommaseo C., Rihs S., Geoffroy N., Chateigner D., Schlegel M., Tisserand D.,
579 Marcus M.A., Tamura N., and Chen Z.S. (2005) Natural speciation of Mn, Ni, and Zn
580 at the micrometer scale in a clayey paddy soil using X-ray fluorescence, absorption,
581 and diffraction. *Geochim. Cosmochim. Acta* **69**, 4007-4034.

582 Manceau A., Kersten M., Marcus M.A., Geoffroy N., and Granina L. (2007a) Ba and Ni
583 speciation in a nodule of binary Mn oxide phase composition from Lake Baikal.
584 *Geochim. Cosmochim. Acta* **71**, 1967-1981.

585 Manceau A., Lanson M., and Geoffroy N. (2007b) Natural speciation of Ni, Zn, Ba, and As in
586 ferromanganese coatings on quartz using X-ray fluorescence, absorption, and
587 diffraction. *Geochim. Cosmochim. Acta* **71**, 95-128.

588 Mandernack K.W., Post J., and Tebo B.M. (1995) Manganese mineral formation by bacterial
589 spores of the marine *Bacillus*, strain SG-1: Evidence for the direct oxidation of Mn(II)
590 to Mn(IV). *Geochim. Cosmochim. Acta* **59**, 4393-4408.

591 Marcus M.A., MacDowell A.A., Celestre R., Manceau A., Miller T., Padmore H.A., and
592 Sublett R.E. (2004a) Beamline 10.3.2 at ALS: a hard X-ray microprobe for
593 environmental and materials sciences. *J. Synchrotron Radiat.* **11**, 239-247.

594 Marcus M.A., Manceau A., and Kersten M. (2004b) Mn, Fe, Zn and As speciation in a fast-
595 growing ferromanganese marine nodule. *Geochim. Cosmochim. Acta* **68**, 3125-3136.

596 McKeown D.A. and Post J.E. (2001) Characterization of manganese oxide mineralogy in rock
597 varnish and dendrites using X-ray absorption spectroscopy. *Amer. Mineral.* **86**, 701-
598 713.

599 Mench M., Bussiere S., Boisson J., Castaing E., Vangronsveld J., Ruttens A., De Koe T.,
600 Bleeker P., Assuncao A., and Manceau A. (2003) Progress in remediation and
601 revegetation of the barren Jales gold mine spoil after in situ treatments. *Plant and Soil*
602 **249**, 187-202.

603 Miyata N., Tani Y., Iwahori K., and Soma M. (2004) Enzymatic formation of manganese
604 oxides by an *Acremonium*-like hyphomycete fungus, strain KR21-2. *FEMS Microbiol.*
605 *Ecol.* **47**, 101-109.

606 Miyata N., Maruo K., Tani Y., Tsuno H., Seyama H., Soma M., and Iwahori K. (2006a)
607 Production of biogenic manganese oxides by anamorphic ascomycete fungi isolated
608 from streambed pebbles. *Geomicrobiol. J.* **23**, 63-73.

609 Miyata N., Tani Y., Maruo K., Tsuno H., Sakata M., and Iwahori K. (2006b) Manganese(IV)
610 oxide production by *Acremonium sp.* strain KR21-2 and extracellular Mn(II) oxidase
611 activity. *Appl. Environ. Microbiol.* **72**, 6467-6473.

612 Nelson Y.M., Lion L.W., Ghiorse W.C., and Shuler M.L. (1999) Production of biogenic Mn
613 oxides by *Leprothrix discophora* SS-1 in a chemically defined growth medium and
614 evaluation of their Pb adsorption characteristics. *Appl. Environ. Microbiol.* **65**, 175-
615 180.

616 Nelson Y.M., Lion L.W., Shuler M.L., and Ghiorse W.C. (2002) Effect of oxide formation
617 mechanisms on lead adsorption by biogenic manganese (hydr)oxides, iron
618 (hydr)oxides, and their mixtures. *Environ. Sci. Technol.* **36**, 421-425.

619 Nelson Y.M. and Lion L.W. (2003) Formation of biogenic manganese oxides and their
620 influence on the scavenging of toxic trace elements. *Geochemical And Hydrological*
621 *Reactivity Of Heavy Metals In Soils*, 169-186.

622 Otte M.L., Rozema J., Koster L., Haarsma M.S., and Broekman R.A. (1989) Iron plaque on
623 roots of *Aster tripolium* L.: Interaction with zinc uptake. *New Phytol.* **111**, 309-317.

624 Panfili F. (2004) Etude de l'évolution de la spéciation du zinc dans la phase solide d'un
625 sédiment de curage contaminé induite par phytostabilisation. Ph.D. thesis, Univ. Aix-
626 Marseille, France, .

627 Panfili F.R., Manceau A., Sarret G., Spadini L., Kirpichtchikova T., Bert V., Laboudigue A.,
628 Marcus M.A., Ahamdach N., and Libert M.F. (2005) The effect of phytostabilization
629 on Zn speciation in a dredged contaminated sediment using scanning electron
630 microscopy, X-ray fluorescence, EXAFS spectroscopy, and principal components
631 analysis. *Geochim. Cosmochim. Acta* **69**, 2265-2284.

632 Plançon A. (2002) CALCIPOW- a program for calculating the diffraction by disordered
633 lamellar structures. *J. Appl. Cryst.* **35**, 377.

634 Römheld V. (1991) The role of phytosiderophores in acquisition of iron and other
635 micronutrients in graminaceous species: an ecological approach. *Plant & Soil* **130**,
636 127-134.

637 Rout G.R. and Das P. (2003) Effect of metal toxicity on plant growth and metabolism: I. Zinc.
638 *Agronomie* **23**, 3-11.

639 Saratovsky I., Wightman P.G., Pasten P.A., Gaillard J.F., and Poepelmeier K.R. (2006)
640 Manganese oxides: Parallels between abiotic and biotic structures. *J. Am. Chem. Soc.*
641 **128**, 11188-11198.

642 Sarret G., Manceau A., Cuny D., VanHaluwyn C., Deruelle S., Hazemann J.L., Soldo Y.,
643 EybertBerard L., and Menthonnex J.J. (1998a) Mechanisms of lichen resistance to
644 metallic pollution. *Environ. Sci. Technol.* **32**, 3325-3330.

645 Sarret G., Manceau A., Spadini L., Roux J.C., Hazemann J.L., Soldo Y., EybertBerard L., and
646 Menthonnex J.J. (1998b) Structural determination of Zn and Pb binding sites in
647 *Penicillium chrysogenum* cell walls by EXAFS spectroscopy. *Environ. Sci. Technol.*
648 **32**, 1648-1655.

649 Sarret G., Saumitou Laprade P., Bert V., Proux O., Hazemann J.L., Traverse A.S., Marcus
650 M.A., and Manceau A. (2002) Forms of zinc accumulated in the hyperaccumulator
651 *Arabidopsis halleri*. *Plant Physiol.* **130**, 1815-1826.

652 Schulze D.G., McCaybuis T., Sutton S.R., and Huber D.M. (1995) Manganese Oxidation-
653 States in *Gaeumannomyces*-Infested Wheat Rhizospheres Probed by Micro-Xanes
654 Spectroscopy. *Phytopathology* **85**, 990-994.

655 Silvester E.J., Manceau A., and Drits V.A. (1997) The structure of monoclinic Na-rich
656 birnessite and hexagonal birnessite. Part 2. Results from Chemical Studies and
657 EXAFS Spectroscopy. *Amer. Mineral.* **82**, 962-978.

658 Simon L. (2005) Stabilization of metals in acidic mine spoil with amendments and red fescue
659 (*Festuca rubra* L.) growth. *Environ. Geochem. Health* **27**, 289-300.

660 Smith R.A.H. and Bradshaw A.D. (1992) Stabilization of toxic mine wastes by the use of
661 tolerant plant populations. *Trans. Inst. Min. Metall.* **81**, A230-A237.

662 St-Cyr L. and Campbell P. (1996) Metals (Fe, Mn, Zn) in root plaque of submerged aquatic
663 plant collected in situ: relations with metal concentrations in adjacent sediments and in
664 the root tissue. *Biogeochemistry* **33**, 45-76.

665 Tani Y., Miyata N., Iwahori K., Soma M., Tokuda S., Seyama H., and Theng B.K.G. (2003)
666 Biogeochemistry of manganese oxide coatings on pebble surfaces in the Kikukawa
667 River System, Shizuoka, Japan. *Appl. Geochem.* **18**, 1541-1554.

668 Tani Y., Miyata N., Ohashi M., Ohnuki T., Seyama H., Iwahori K., and Soma M. (2004)
669 Interaction of inorganic arsenic with biogenic manganese oxide produced by a Mn-
670 oxidizing fungus, strain KR21-2. *Environ. Sci. Technol.* **38**, 6618-6624.

671 Tebo B.M., vanWaasbergen L.G., Francis C.A., He L.M., Edwards D.B., and Casciotti K.
672 (1998) Manganese oxidation by spores of the marine *Bacillus sp.* strain SG-1 -
673 Application for the bioremediation of metal pollution. *New Developments In Marine*
674 *Biotechnology*, 177-180.

675 Tebo B.M., Bargar J.R., Clement B.G., Dick G.J., Murray K.J., Parker D., Verity R., and
676 Webb S.M. (2004) Biogenic manganese oxides: Properties and mechanisms of
677 formation. *Annu. Rev. Earth Planet. Sci.* **32**, 287-328.

678 Teo B.K. (1986) *EXAFS: basic principles and data analysis*. Springer-Verlag.

679 Thompson I.A., Huber D.M., Guest C.A., and Schulze D.G. (2005) Fungal manganese
680 oxidation in a reduced soil. *Environ. Microbiol.* **7**, 1480-1487.

681 Thompson I.A., Huber D.M., and Schulze D.G. (2006) Evidence of a multicopper oxidase in
682 Mn oxidation by *Gaeumannomyces graminis* var. *tritici*. *Phytopathology* **96**, 130-136.

683 Toner B., Fakra S., Villalobos M., Warwick T., and Sposito G. (2005a) Spatially resolved
684 characterization of biogenic manganese oxide production within a bacterial biofilm.
685 *Appl. Environ. Microbiol.* **71**, 1300-1310.

686 Toner B., Manceau A., Marcus M.A., Millet D.B., and Sposito G. (2005b) Zinc sorption by a
687 bacterial biofilm. *Environ. Sci. Technol.* **39**, 8288-8294.

688 Toner B., Manceau A., Webb S.M., and Sposito G. (2006) Zinc sorption to biogenic
689 hexagonal-birnessite particles within a hydrated bacterial biofilm. *Geochim.*
690 *Cosmochim. Acta* **70**, 27-43.

691 Vangronsveld J., Van Assche F., and Clijsters H. (1995) Reclamation of a bare industrial area
692 contaminated by non-ferrous metals: *In situ* metal immobilization and revegetation.
693 *Environ. Pollut.* **87**, 51-59.

694 Villalobos M., Toner B., Bargar J., and Sposito G. (2003) Characterization of the manganese
695 oxide produced by *Pseudomonas putida* strain MnB1. *Geochim. Cosmochim. Acta* **67**,
696 2649-2662.

697 Villalobos M., Bargar J.R., and Sposito G. (2005) Mechanisms of Pb(II) sorption on a
698 biogenic manganese oxide. *Environ. Sci. Technol.* **39**, 569-576.

699 Villalobos M., Lanson B., Manceau A., Toner B., and Sposito G. (2006) Structural model for
700 the biogenic Mn oxide produced by *Pseudomonas putida*. *Amer. Mineral.* **91**, 489-
701 502.

702 Wadsley A.D. (1955) The crystal structure of chalcophanite, $ZnMn_3O_7 \cdot 3H_2O$. *Acta*
703 *Crystallogr.* **8**, 165-172.

704 Warren B.E. (1941) X-ray diffraction in random layer lattices. *Phys. Rev.* **59**, 693-698.

705 Webb S.M., Tebo B.M., and Bargar J.R. (2005a) Structural characterization of biogenic Mn
706 oxides produced in seawater by the marine *Bacillus sp.* strain SG-1. *Amer. Mineral.*
707 **90**, 1342-1357.

708 Webb S.M., Tebo B.M., and Bargar J.R. (2005b) Structural influences of sodium and calcium
709 ions on the biogenic manganese oxides produced by the marine *Bacillus sp.*, strain
710 SG-1. *Geomicrobiol. J.* **22**, 181-193.

711

712

FIGURE CAPTIONS

713
714
715
716
717
718
719
720
721
722
723
724
725
726
727
728
729
730
731
732
733
734
735
736
737

Fig. 1. Roots of *Festuca rubra* grown on a Zn-contaminated sediment. Optical microphotograph (a), and scanning electron microscope image with (b) backscattered electrons and (c) secondary electrons.

Fig. 2. Tricolor (RGB) μ -XRF map of a root with Mn-Zn precipitates. Red codes for Ca, green for Zn, and blue for Mn. Each pixel is colored in proportion to Ca-, Zn- and Mn-K α signals. Pixel size is $7 \times 7 \mu\text{m}^2$. The graph is a pixel-by-pixel scatterplot of Zn counts vs. Mn counts, showing the constant Zn:Mn ratio.

Fig. 3. Manganese K-edge EXAFS spectra of Mn-Zn precipitate (dotted lines) and the following references (solid lines): hollandite (Hol), todorokite (Todo), triclinic birnessite (TcBi), lithiophorite (Lit), low-pH hexagonal birnessite (HBi), chalcophanite (Chalco), and δ -MnO₂ (dBi, synthetic turbostratic birnessite).

Fig. 4. Fourier transforms (FTs) of the k -weighted Mn-EXAFS spectra for the Mn-Zn precipitate (dotted lines) and synthetic ^{VI}Zn-sorbed δ -MnO₂ (dBi), chalcophanite (Chalco), hexagonal birnessite (HBi), and lithiophorite (Lit). E and TC subscripts denote Mn-Mn contributions from octahedral linked by edges and triple-corners, respectively.

Fig. 5. Zinc K-edge EXAFS spectra. (a-c) Overlay plots of the Mn-Zn precipitate spectrum (dotted line) with natural ^{IV}Zn-containing turbostratic birnessite (vernadite, sample 6KR) from Manceau et al. (2007b; a, solid line – Sum-sq = 0.12), ^{VI/IV}Zn-sorbed δ -MnO₂ (dBi) from Toner et al. (2006; b, solid line – Sum-sq = 0.83), and a least-squares fit of the Mn-Zn precipitate spectrum to a linear combination of the model compounds in (a) and (b) (c, solid line – Sum-sq = 0.06). The arrows in (a) point out the phase misfit when the ^{VI}TC Zn species is omitted in the simulation. The dBi

738 sample contains 42 (± 5) mol% ^{IV}TC Zn and 58 (± 5) mol% ^{VI}TC Zn (Toner et al.,
739 2006). Substituting chalcophanite for dBi in the two-component fit yielded the same
740 fraction of TC species and a similar Sum-sq residual (0.07). **(d)** Overlay plot of the
741 Mn-Zn precipitate spectrum (dotted line) and of the Root spectrum (solid line – Sum-
742 sq = 0.10). **(e-g)** Overlay plots of the Root spectrum (dotted line) with organic model
743 compounds (solid line): Zn sorbed on a biofilm at $5.6 \cdot 10^{-4}$ mol of Zn per gram of
744 biosorbent from Toner et al. (2005b; **e**, Zncell7 – Sum-sq = 0.052), Zn citrate from
745 Sarret et al. (2002; **f**, – Sum-sq = 0.089), Zn phytate from Sarret et al. (2002; **g**, –
746 Sum-sq = 0.089), Zn sorbed on *Penicillium chrysogenum* at $1.5 \cdot 10^{-4}$ mol of Zn per
747 gram of biosorbent from Sarret et al. (1998b; **h**, – Sum-sq = 0.13). The Sum-sq
748 values are calculated as the squares of the residuals, normalized to the sum of the
749 squares of the data values over the $[3.0 - 10.5 \text{ \AA}^{-1}]$ k interval.

750 **Fig. 6.** XRD pattern of Mn-Zn precipitate after subtraction of the scattering from the root.

751 **Fig. 7.** Simulations of the $[20,11]$ and $[02,31]$ X-ray scattering bands (C-centered layer cell).

752 Black crosses are experimental data, and red lines are calculated profiles. Small but
753 significant misfits between experimental and calculated patterns are pointed out with
754 arrows. Diffracted intensities were calculated with a turbostratic layer stacking (no
755 interlayer correlation). **(a)** Initial model with 0.186 vacant layer sites and no
756 interlayer Mn. **(b)** Optimal model (Table 1; Figs. 8 and EA-5). **(c)** Model with $a =$
757 5.014 \AA and $b = 2.895 \text{ \AA}$ (hexagonal layer symmetry). **(d)** Model with $a = 5.100 \text{ \AA}$
758 and $b = 2.850 \text{ \AA}$ (orthogonal layer symmetry). **(e)** Model with all interlayer Mn
759 cations (0.056 per octahedron) located in ^{VI}TC sites, instead of 0.046 and 0.010 in
760 ^{VI}TE and ^{VI}TC sites, respectively, in the optimal fit. **(f)** Model with 0.240 Ca per
761 layer octahedron instead of 0.318 in the optimal model. **(g)** Model with 0.150 vacant
762 sites and 0.244 interlayer Zn^{2+} (Zn:Mn = 0.27), compared to 0.220 and 0.388

763 (Zn:Mn = 0.46) in the optimal fit. **(h)** Model with 50% tetrahedral and 50%
764 octahedral Zn^{2+} , instead of 77% and 23% in the optimal fit. Unless specified, all
765 parameters used in calculations are those of the optimal model.

766 **Fig. 8.** Idealized structure for the Mn-Zn root precipitate with structural formula
767 $[(Mn_{0.78}Vac_{0.22})O_2]Mn^{VITC}_{0.010}Mn^{VITE}_{0.046}Zn^{VITC}_{0.088}Zn^{IVTC}_{0.300}Ca_{0.318}(H_2O)_{0.972}$. The
768 layer charge deficit due to vacant layer sites is balanced by interlayer Zn and Mn
769 above and/or below layer vacancies, and by Ca in the interlayer mid-plane (see Fig.
770 EA-5 for details).

771 **Fig. 9.** Calculation of the 001 and 002 reflections for crystallites composed of one (dashed
772 line), two (dotted-dashed line) and three (dot-dot-dashed line) parallel layers
773 randomly stacked perpendicular to the *ab* plane, and optimal fit (red line) to the data
774 (crosses) obtained with an assemblage of diffracting particles containing 1, 2, and 3
775 layers in the ratio of 2.0:0.3:0.1. Atomic coordinates of the optimal structure model,
776 derived from the simulation of the [20,11] and [02,31] reflections, were used in all
777 calculations (Figs. 7b and 8, Table 1).

Table 1. Structural parameters of Mn-Zn precipitate derived from the simulation of XRD data.

Atom	x	y	ζ	Occ.	x	y	ζ	Occ.
Mn _{layer} (Mn1)	0	0	0	0.780	-	-	-	-
O _{layer} (O1)	0.333	0	1.00	1.00	-0.333	0	-1.00	1.00
^{TC} Mn _{inter} (Mn2)	0	0	2.20	0.005	0	0	-2.20	0.005
H ₂ O _{inter} . (O2)	-0.333	0	3.45	0.015	0.333	0	-3.45	0.015
^{TE} Mn _{inter} (Mn3)	-0.333	0	2.20	0.023	0.333	0	-2.20	0.023
H ₂ O _{inter} . (O3)	0	0	3.45	0.069	0	0	-3.45	0.069
^{VI} Zn _{inter} (Zn1)	0	0	2.20	0.044	0	0	-2.20	0.044
H ₂ O _{inter} . (O2)	-0.333	0	3.45	0.132	0.333	0	-3.45	0.132
^{IV} Zn _{inter} (Zn2)	0	0	1.77	0.150	0	0	-1.77	0.150
H ₂ O _{inter} . (O4)	0	0	3.70	0.150	0	0	-3.70	0.150
Ca _{inter} (Ca1)	-0.410	0	3.60	0.053	0.410	0	-3.60	0.053
Ca _{inter} (Ca1)	-0.295	0.115	3.60	0.053	0.295	0.115	-3.60	0.053
Ca _{inter} (Ca1)	-0.295	-0.115	3.60	0.053	0.295	-0.115	-3.60	0.053
H ₂ O _{inter} . (O5)	0.220	0	3.60	0.04	-0.220	0	-3.60	0.04
H ₂ O _{inter} . (O5)	-0.110	0.330	3.60	0.04	-0.110	-0.330	-3.60	0.04
H ₂ O _{inter} . (O5)	-0.110	-0.330	3.60	0.04	0.110	-0.330	-3.60	0.04

Note: $b = 2.850 \text{ \AA}$, $a = b\sqrt{3} = 4.936 \text{ \AA}$, $\gamma = 90^\circ$, and $d_{(001)} = 7.20 \text{ \AA}$. x and y coordinates are

expressed as fractions of the a and b parameters, respectively. Coordinates along the c^*

axis, ζ , are expressed in Å to point out the thickness of layer and interlayer polyhedra. The average dimension of the coherent scattering domains (CSDs) along the c^* axis is 1.2 layers (8.6 Å). The average radius of the disk-like CSDs in the ab plane is 33 Å. This value was calculated by fitting the [20,11] reflection. Un-refined thermal B factors are 0.5 \AA^2 for Mn_{layer} , 1.0 \AA^2 for O_{layer} , interlayer Mn, and interlayer Zn, and 2.0 \AA^2 for Ca^{2+} and H_2O .

Table 2. Selected interatomic distances for the optimal structure model.

Atomic pair	Distance (Å)	Atomic pair	Distance (Å)
$\text{Mn}_{\text{layer}}\text{-O}_{\text{layer}}$	1.925		
$^{\text{TC,TE}}\text{Mn}_{\text{inter.}}\text{-O}_{\text{layer}}$	2.04	$^{\text{TC,TE}}\text{Mn}_{\text{inter.}}\text{-H}_2\text{O}$	2.07
$^{\text{VI}}\text{Zn}_{\text{inter.}}\text{-O}_{\text{layer}}$	2.04	$^{\text{VI}}\text{Zn}_{\text{inter.}}\text{-H}_2\text{O}$	2.07
$^{\text{IV}}\text{Zn}_{\text{inter.}}\text{-O}_{\text{layer}}$	1.82 ^a	$^{\text{IV}}\text{Zn}_{\text{inter.}}\text{-H}_2\text{O}$	1.93
$\text{Ca}_{\text{inter.}}\text{-O}_{\text{layer}}$	2.89	$\text{H}_2\text{O}_{\text{inter.}}\text{-O}_{\text{layer}}$	2.66
$\text{Mn}_{\text{layer}}\text{-}^{\text{VI}}\text{Zn}_{\text{inter}}$	3.60	$\text{Mn}_{\text{layer}}\text{-}^{\text{IV}}\text{Zn}_{\text{inter}}$	3.35
$\text{Mn}_{\text{layer}}\text{-}^{\text{TC}}\text{Mn}_{\text{inter.}}$	3.60	$\text{Mn}_{\text{layer}}\text{-}^{\text{TE}}\text{Mn}_{\text{inter.}}$	2.75 ^b

^(a) The $^{\text{IV}}\text{Zn}_{\text{inter.}}\text{-O}_{\text{layer}}$ distance should be increased by $\sim 0.1 \text{ \AA}$ to provide more realistic Zn-O bond valence (Table EA-1). This cannot be achieved by changing the z coordinate of $^{\text{IV}}\text{Zn}$ (Fig. EA-6b). Alternatively, moving apart the three oxygen atoms delimiting the underlying vacancy by 0.15 \AA in the [110], $[\bar{1}00]$, and $[0\bar{1}0]$ directions increases the $^{\text{IV}}\text{Zn}_{\text{inter.}}\text{-O}_{\text{layer}}$ distance from 1.82 \AA to 1.95 \AA , as discussed in Manceau et al. (2002a).

(b) The $\text{Mn}_{\text{layer}}^{\text{TE}}\text{Mn}_{\text{inter}}$ distance can be increased by $\sim 0.1 \text{ \AA}$ by shifting Mn_{inter} in the ab plane from its ideal TE position towards the nearest vacant site (see Fig. EA-5). This shift occurs along the $a \pm 120^\circ$ directions with equal probabilities resulting in an increased Debye-Waller B factor without significant alteration of the fit quality.

Table EA-1. Empirical bond-valences for Mn-Zn precipitate^a.

	O1 ^b	O1 ^c	O1 ^d	O1 ^e	O2, O3	O3	O4	Σ	Formal valence
Mn1	0.628 ×6→ ×3↓	0.628 ×2↓	0.628 ×2↓	0.628 ×2↓				3.8	4
Mn2, Mn3		0.469 ×3→			0.433 ×3→			2.7	3
Zn1			0.403 ×3→			0.372 ×3→		2.3	2
Zn2				0.731 ×3→			0.543	2.7	2
H ⁺	0.11 ^f								
Σ	1.9 – 2.0 ^g	1.7	1.7	2.0					

^(a) Bond valences in valence unit (v.u.) were calculated using the Valence for Dos program (v. 2.0 - http://www.ccp14.ac.uk/solution/bond_valence/index.html) and the parameters from Brese and O' Keeffe (1991).

^(b) O1 coordinated to 3 Mn⁴⁺ in Mn1 (Table 1).

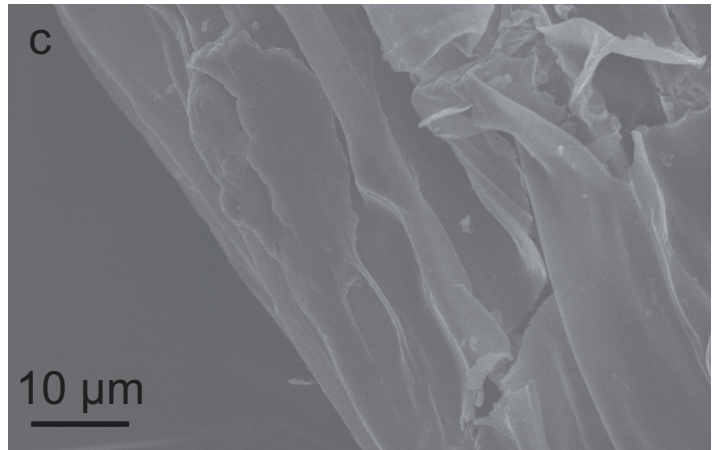
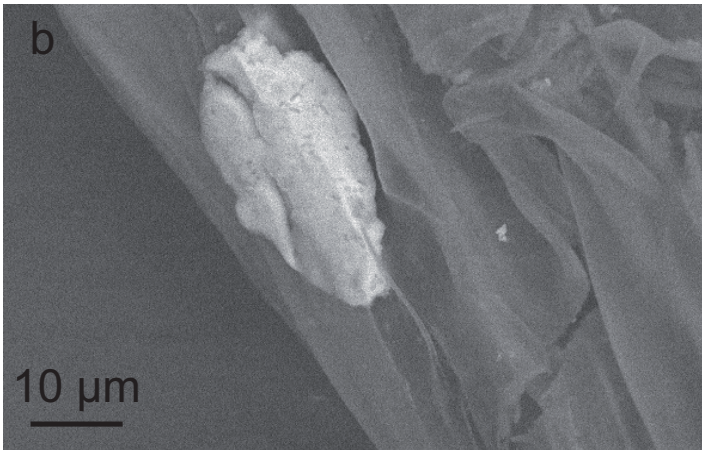
^(c) O1 coordinated to 2 Mn⁴⁺ in Mn1 and 1 Mn³⁺ in Mn2 or Mn3.

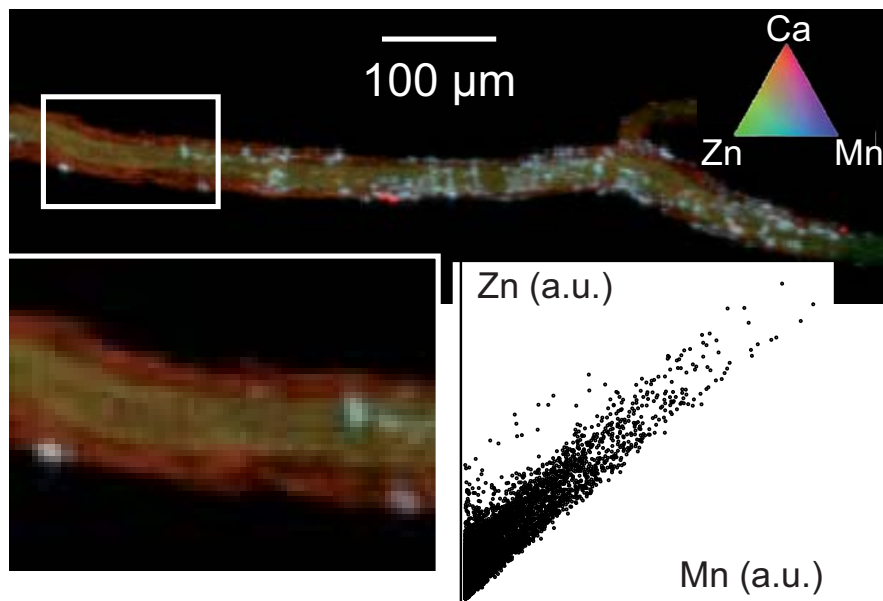
^(d) O1 coordinated to 2 Mn⁴⁺ in Mn1 and 1 Zn²⁺ in Zn1.

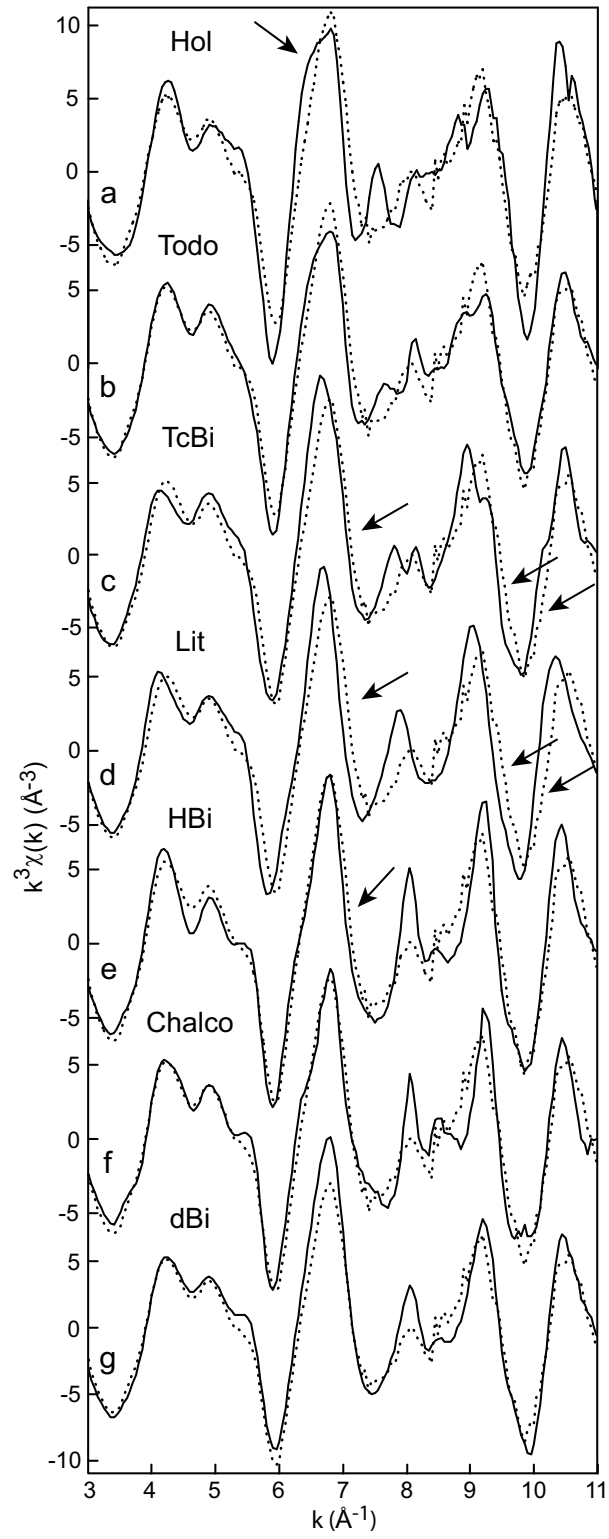
^(e) O1 coordinated to 2 Mn⁴⁺ in Mn1 and 1 Zn²⁺ in Zn2.

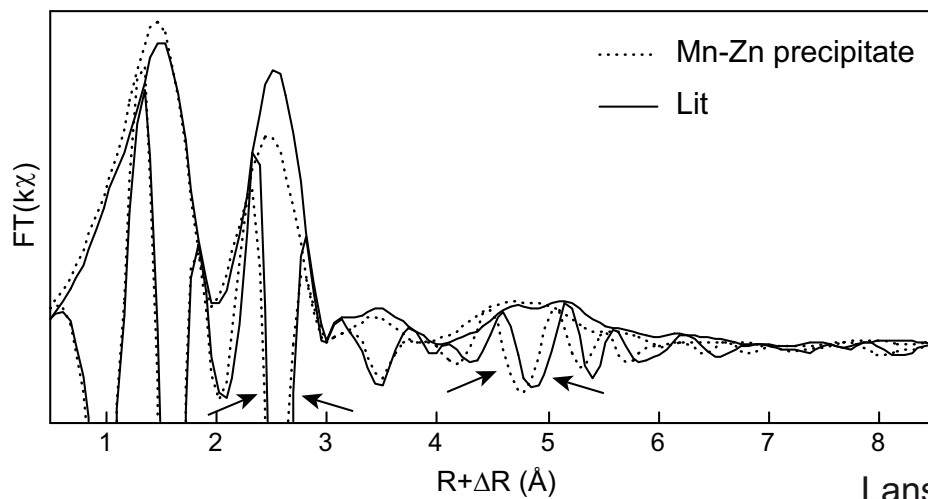
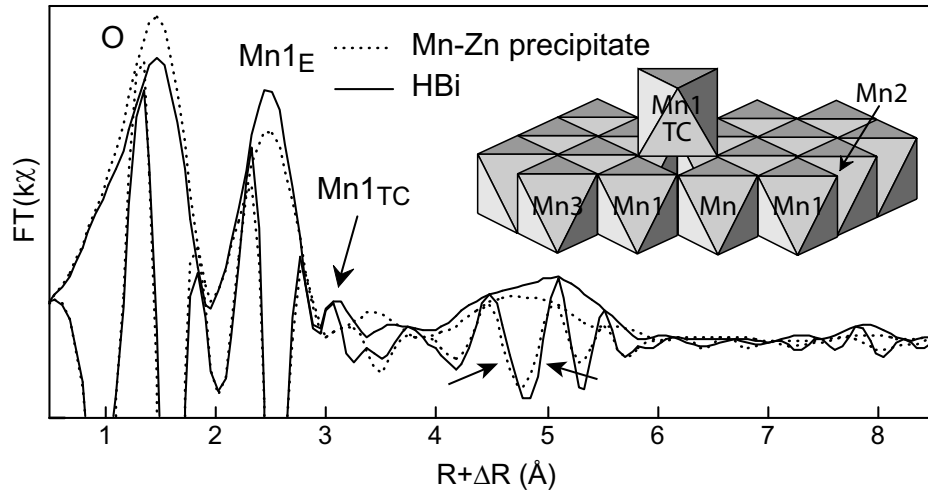
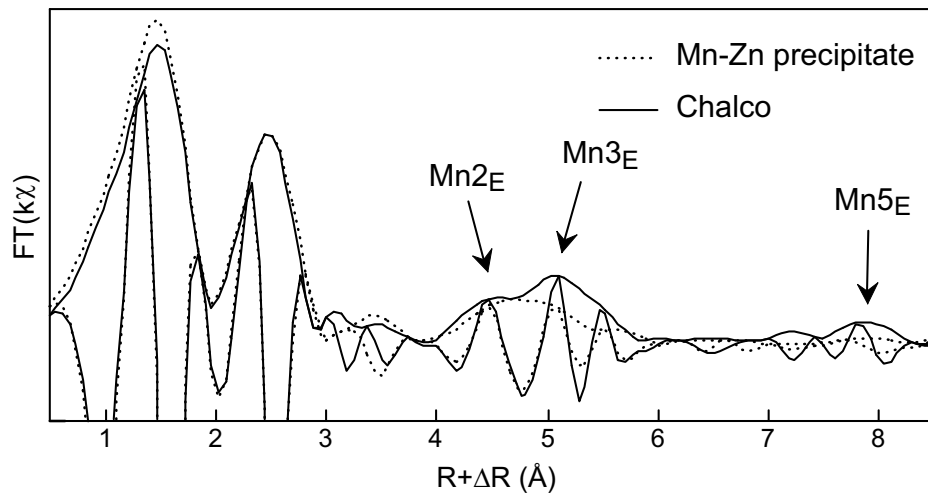
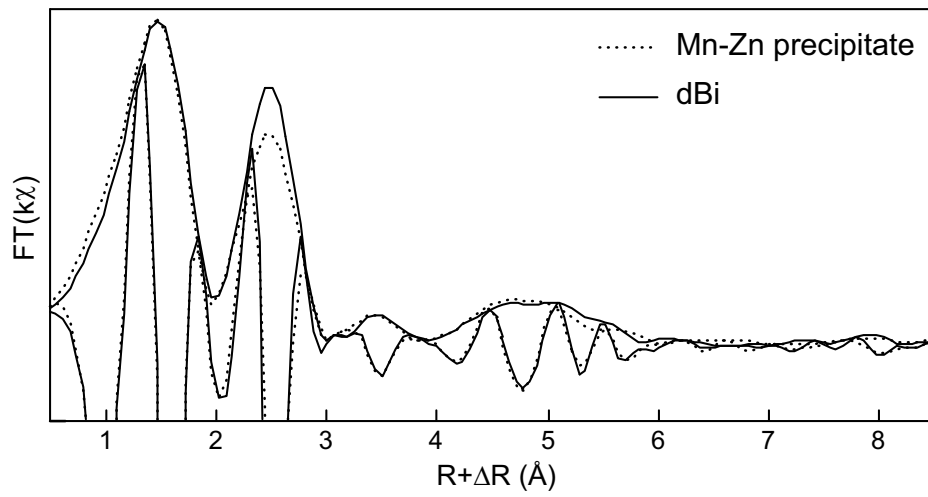
^(f) O5-H-O1 H-bond.

^(g) Depending on whether this O1 receives additional valence from H⁺ through H-bond.

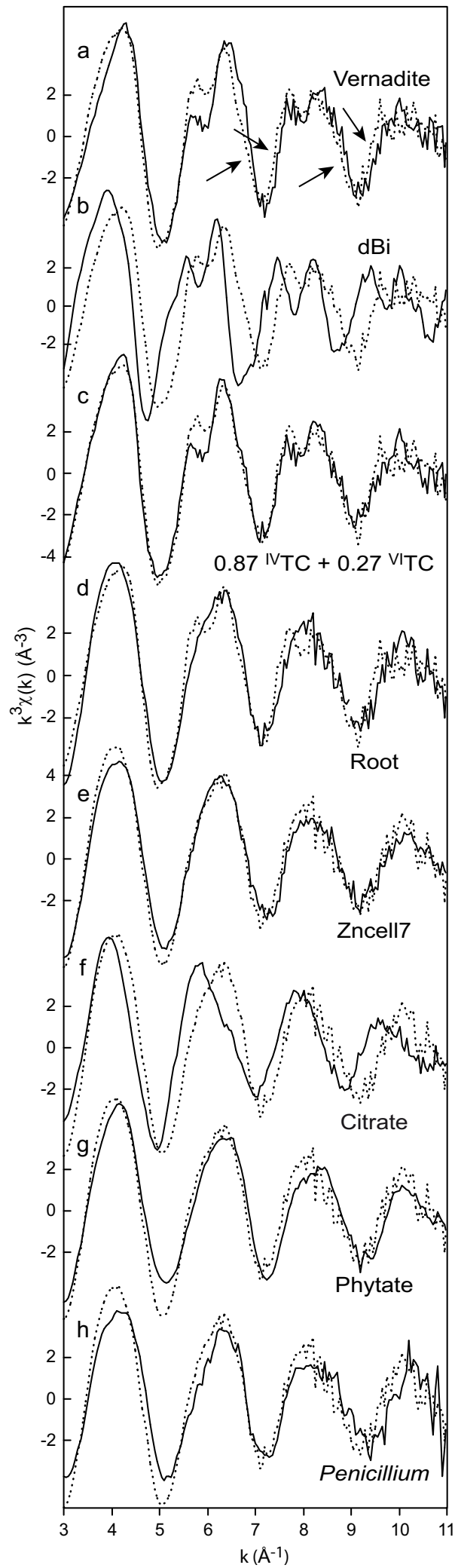




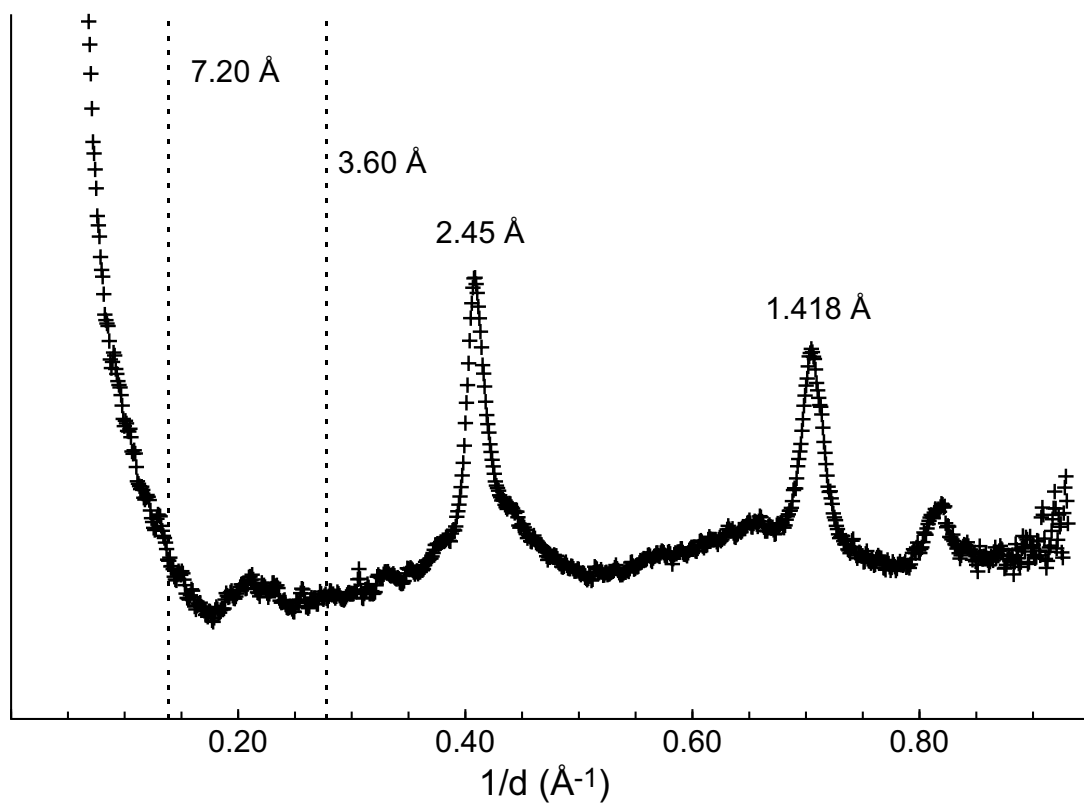


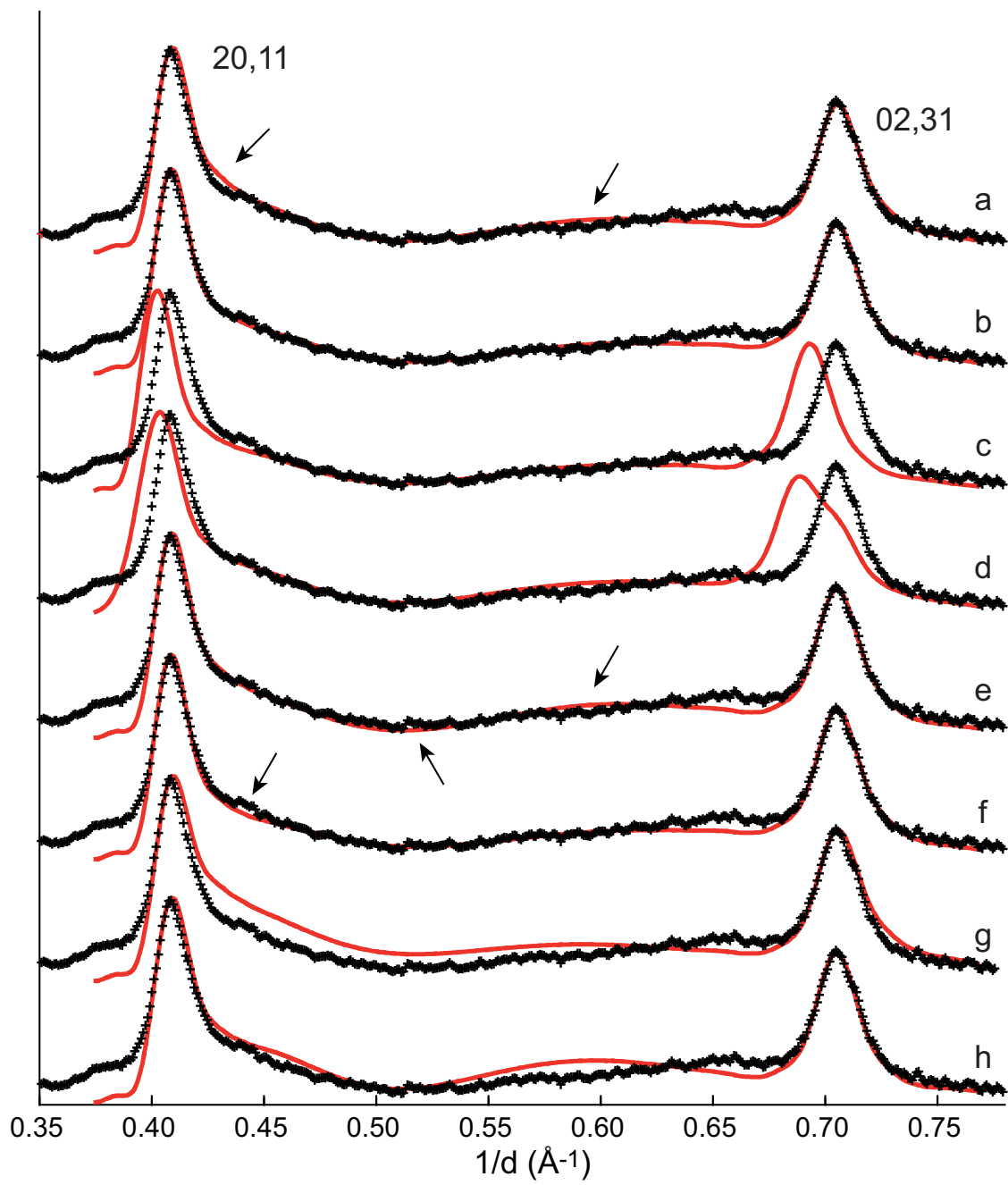


Lanson et al., Fig. 4

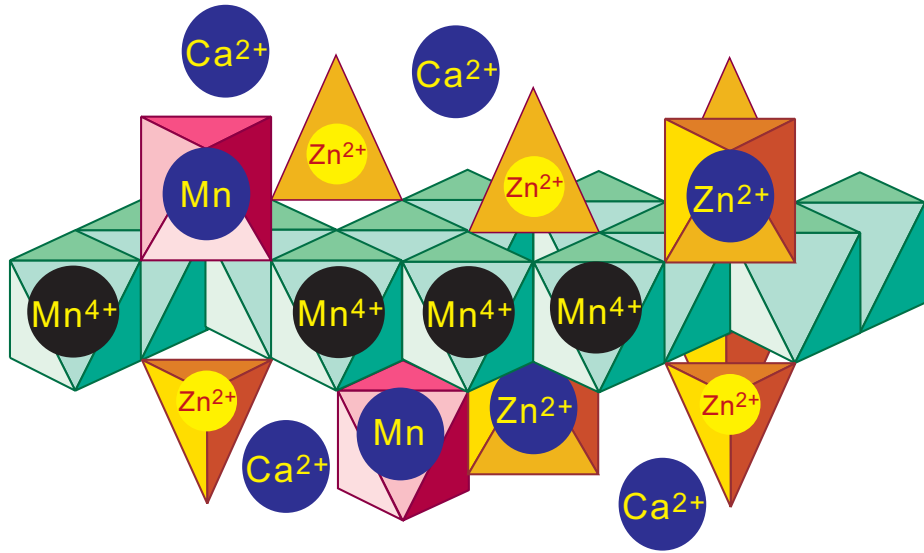


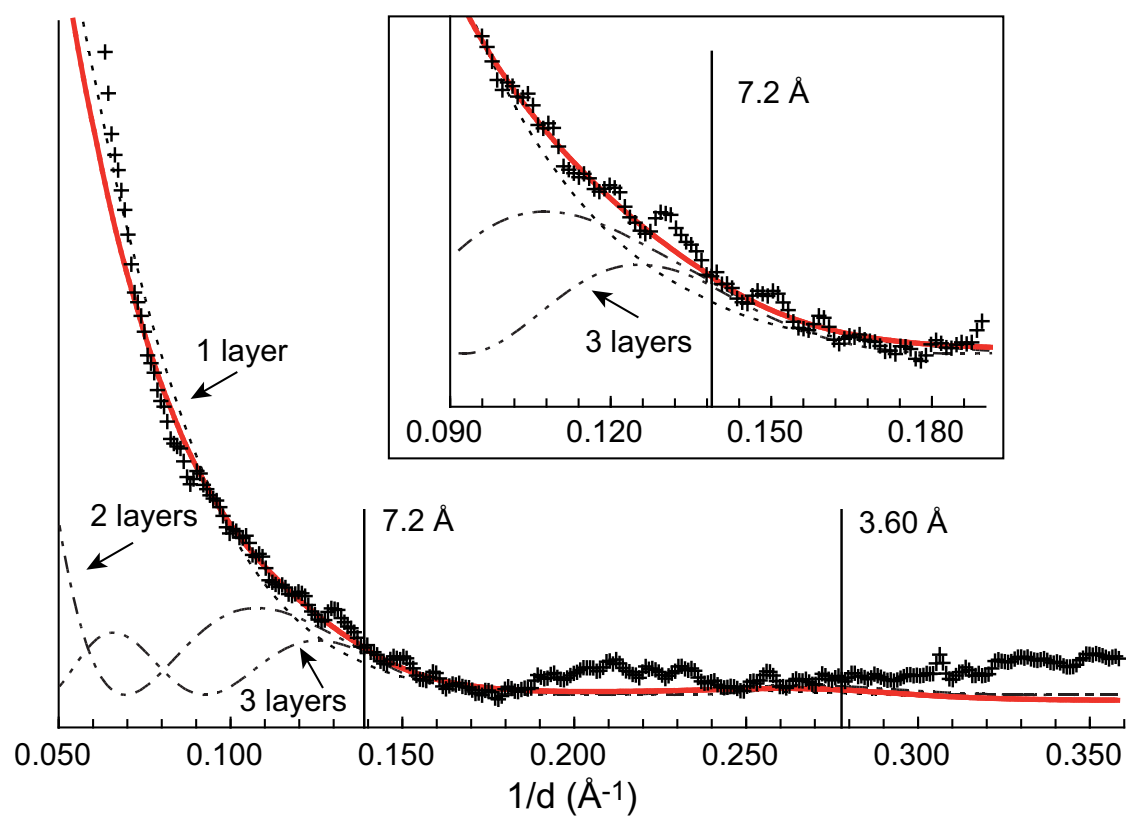
Lanson et al., Fig. 5





Lanson et al., Fig. 7





Lanson et al., Fig. 9

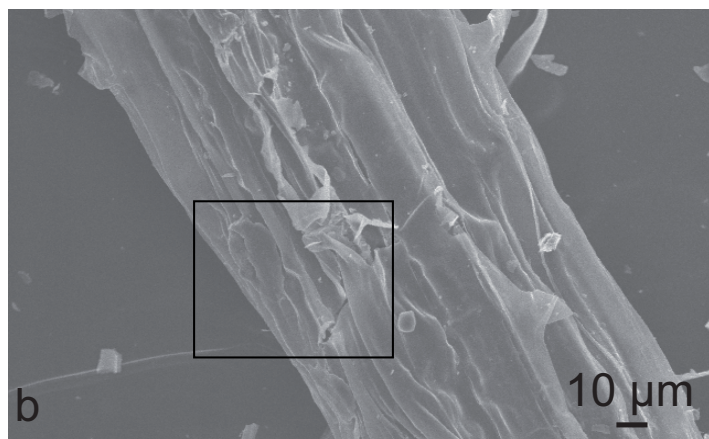
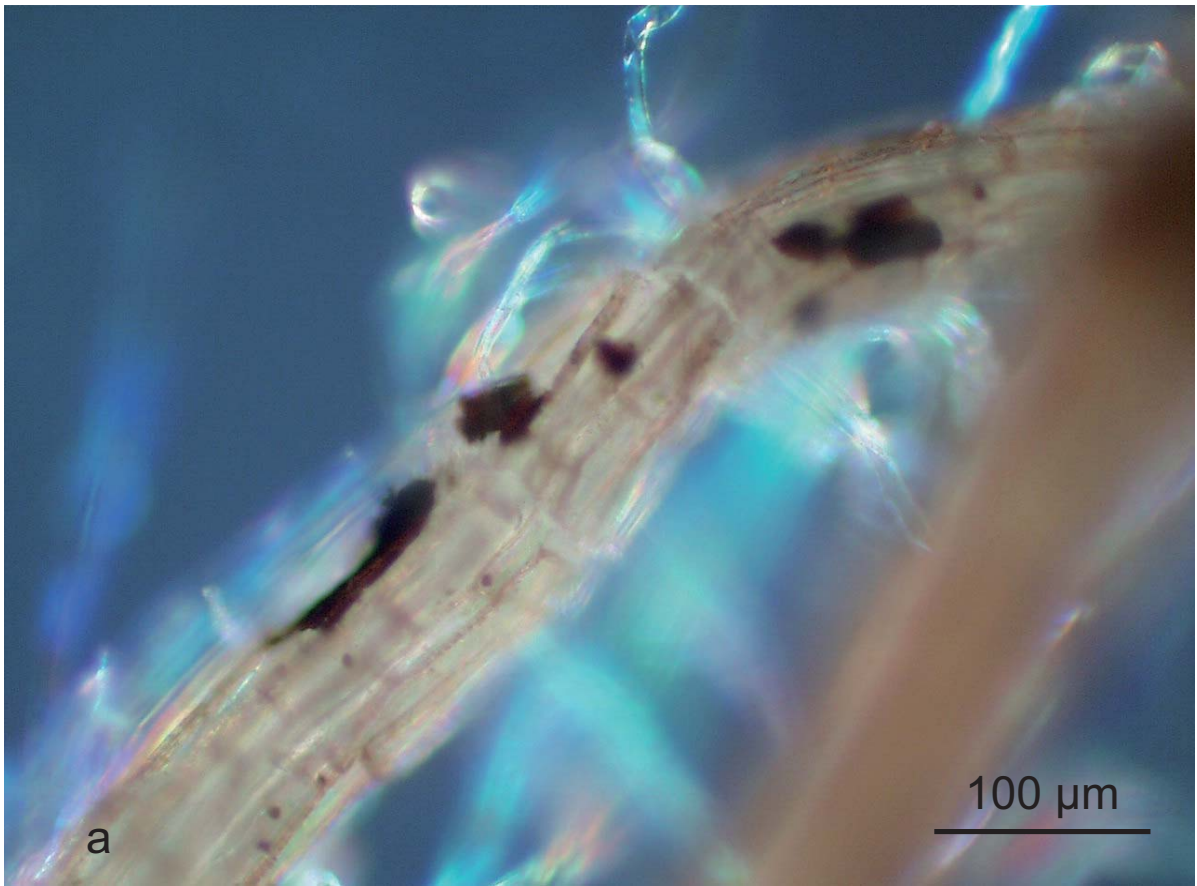


Fig. EA-1: Roots of *Festuca rubra* grown on a Zn-contaminated sediment. (a) Close-up photograph from Fig. 1a. (b) Lower magnification of Fig. 1c.

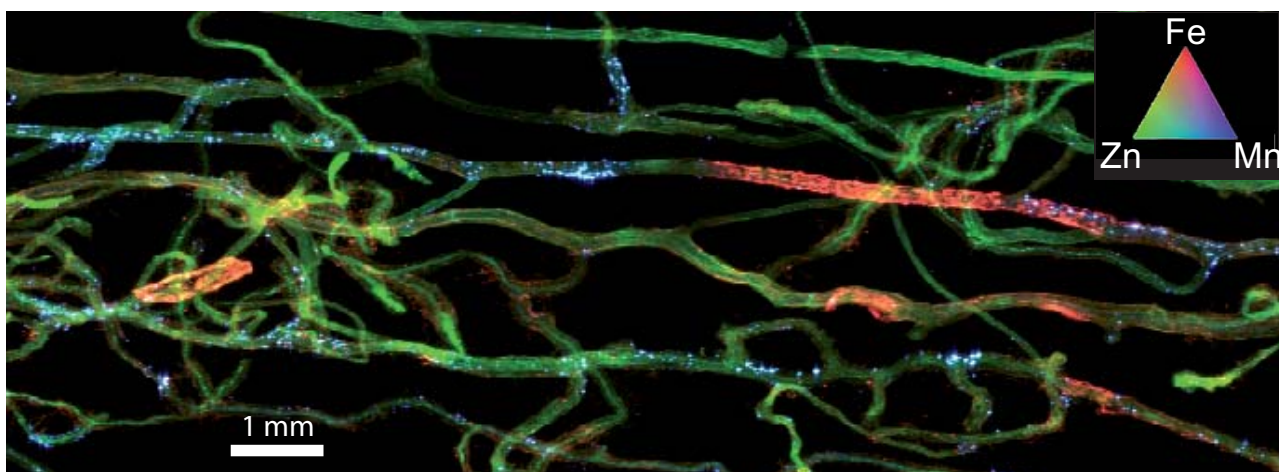


Fig. EA-2: Tricolor (RGB) μ -XRF map of a bundle of roots. Red codes for Fe, green for Zn, and blue for Mn. Each pixel is colored in proportion to Fe-, Zn- and Mn-K α signals. Pixel size is $18 \times 15 \mu\text{m}^2$.

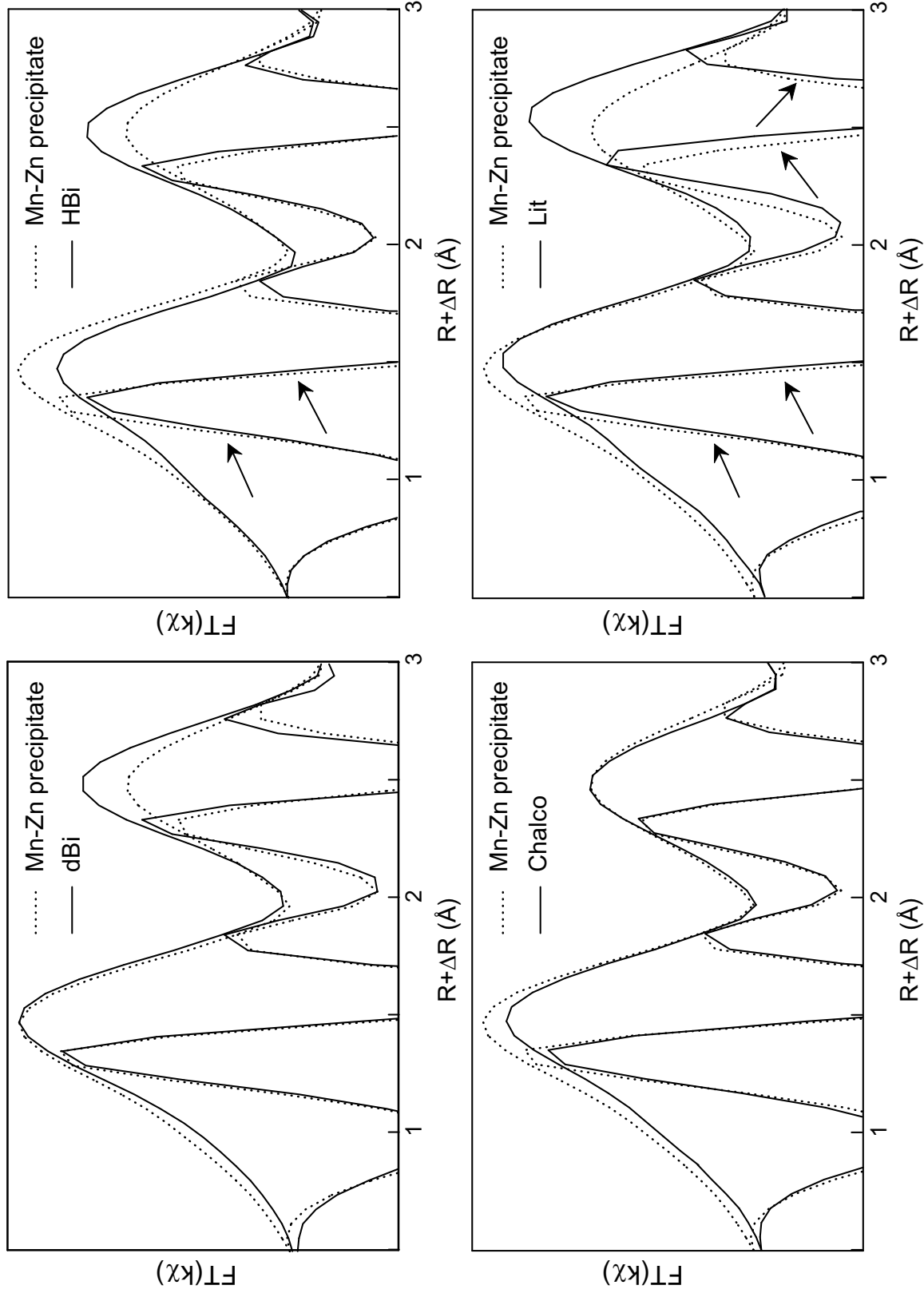


Fig. EA-3: Fourier transforms (FTs) of the manganese K-edge k -weighted EXAFS spectra for the Mn-Zn root precipitate and synthetic ^{51}Zn -sorbed $\delta\text{-MnO}_2$ (dBi, synthetic turbostratic birnessite), chalcophanite (Chalco), hexagonal birnessite (HBi), and lithiophorite (Lit). Expansion of the [1-3 Å] $R+\Delta R$ interval.

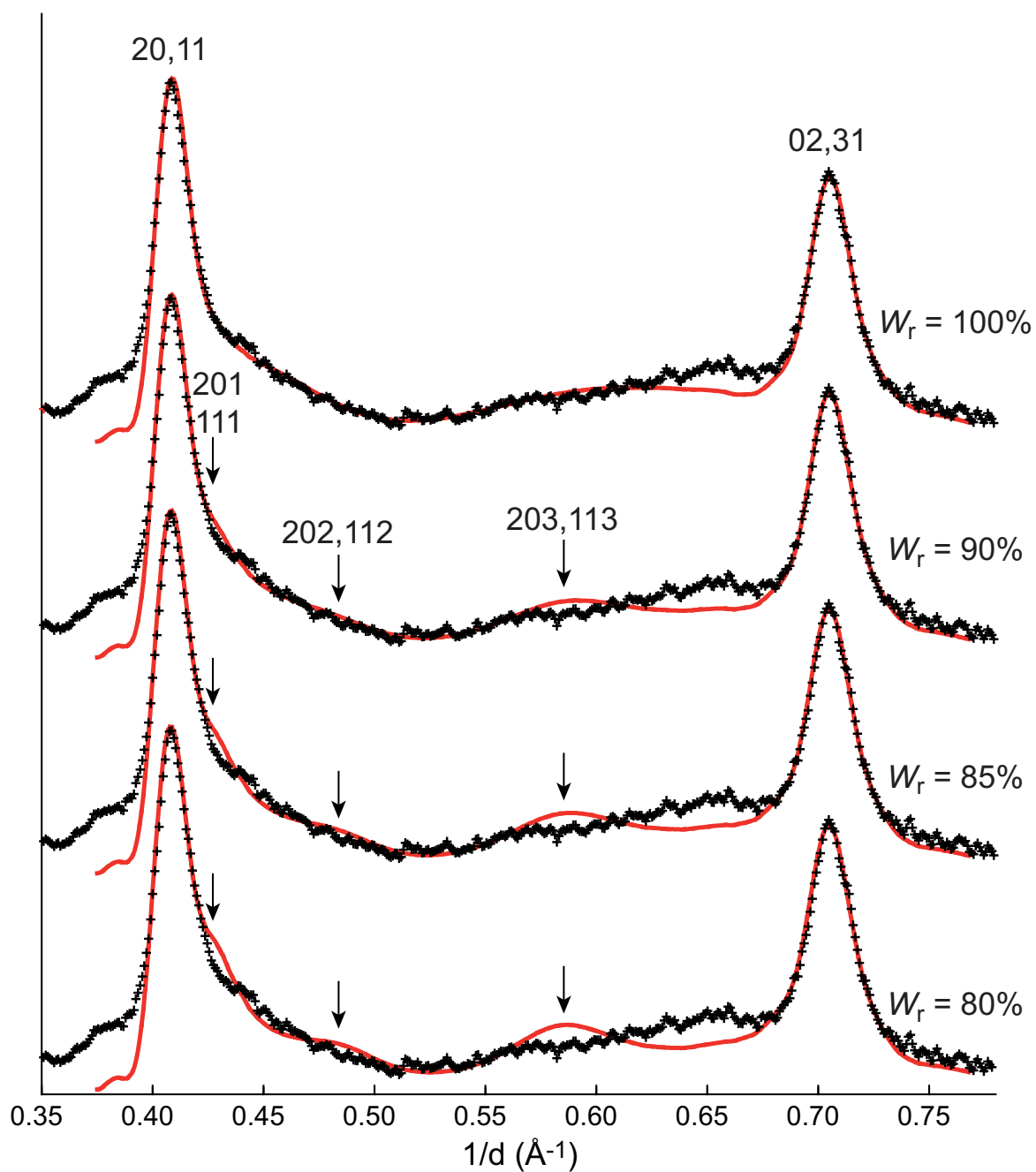


Fig. EA-4: Simulations of the $[20,11]$ and $[02,31]$ X-ray scattering bands (black crosses, C-centered layer cell). Intensities (red lines) were calculated for the optimal structure model (Table 1) with different occurrence probabilities of random stacking faults (W_r). Arrows indicate the positions of hkl reflections.

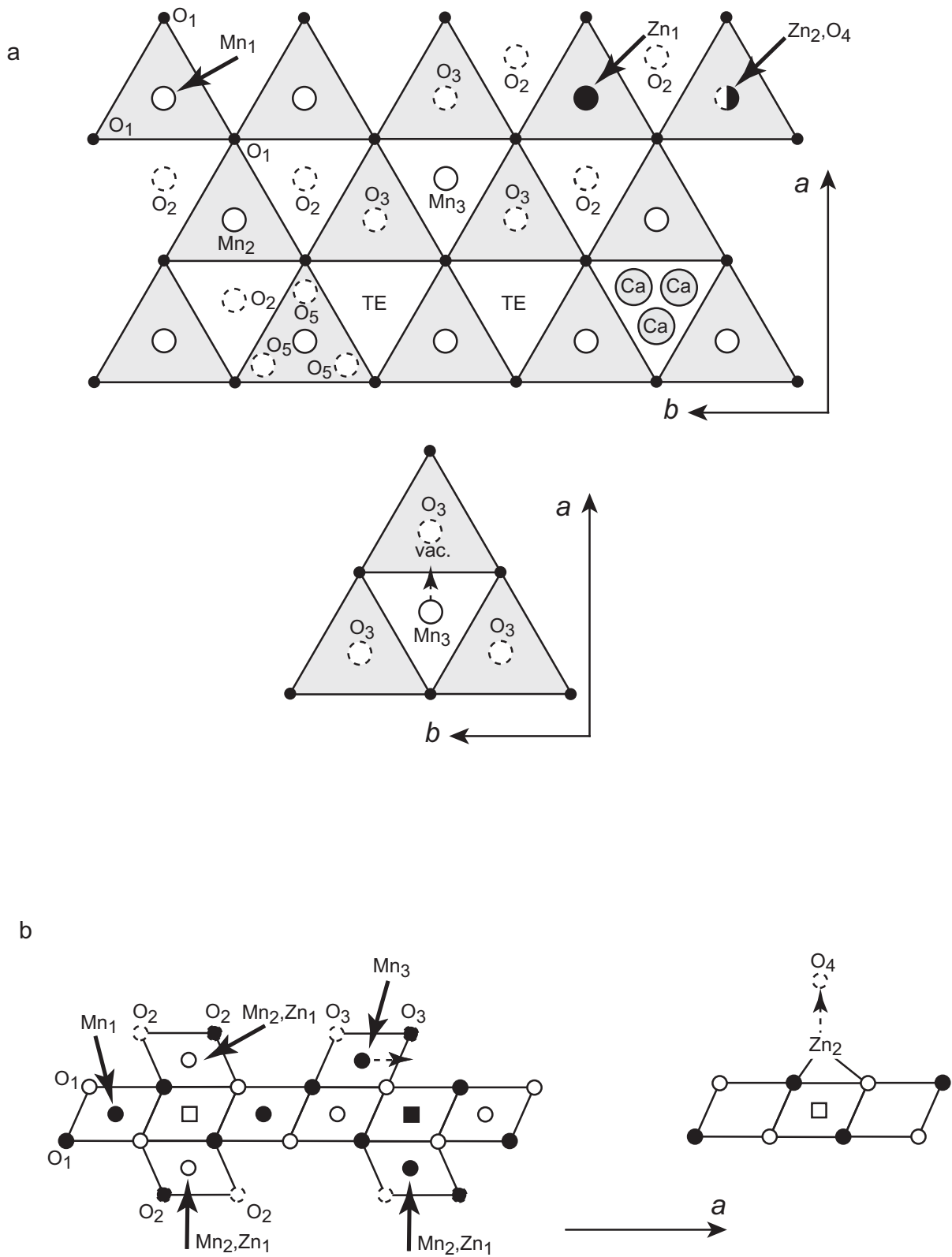


Fig. EA-5: Idealized structure of Mn-Zn precipitate. (a) Projection on the ab plane. The upper surface of the layer is shown as light shaded triangles, and the atomic notations are the same as in Table 1. (b) Projection along the b axis. Open and solid symbols indicate atoms at $y = 0$ and $y = \pm 1/2$, respectively. Squares represent vacant layer octahedra. The Mn_3 and Zn_2 atoms can be shifted from their positions as indicated by the dashed arrows to obtain more realistic interatomic distances (see Table EA-1).

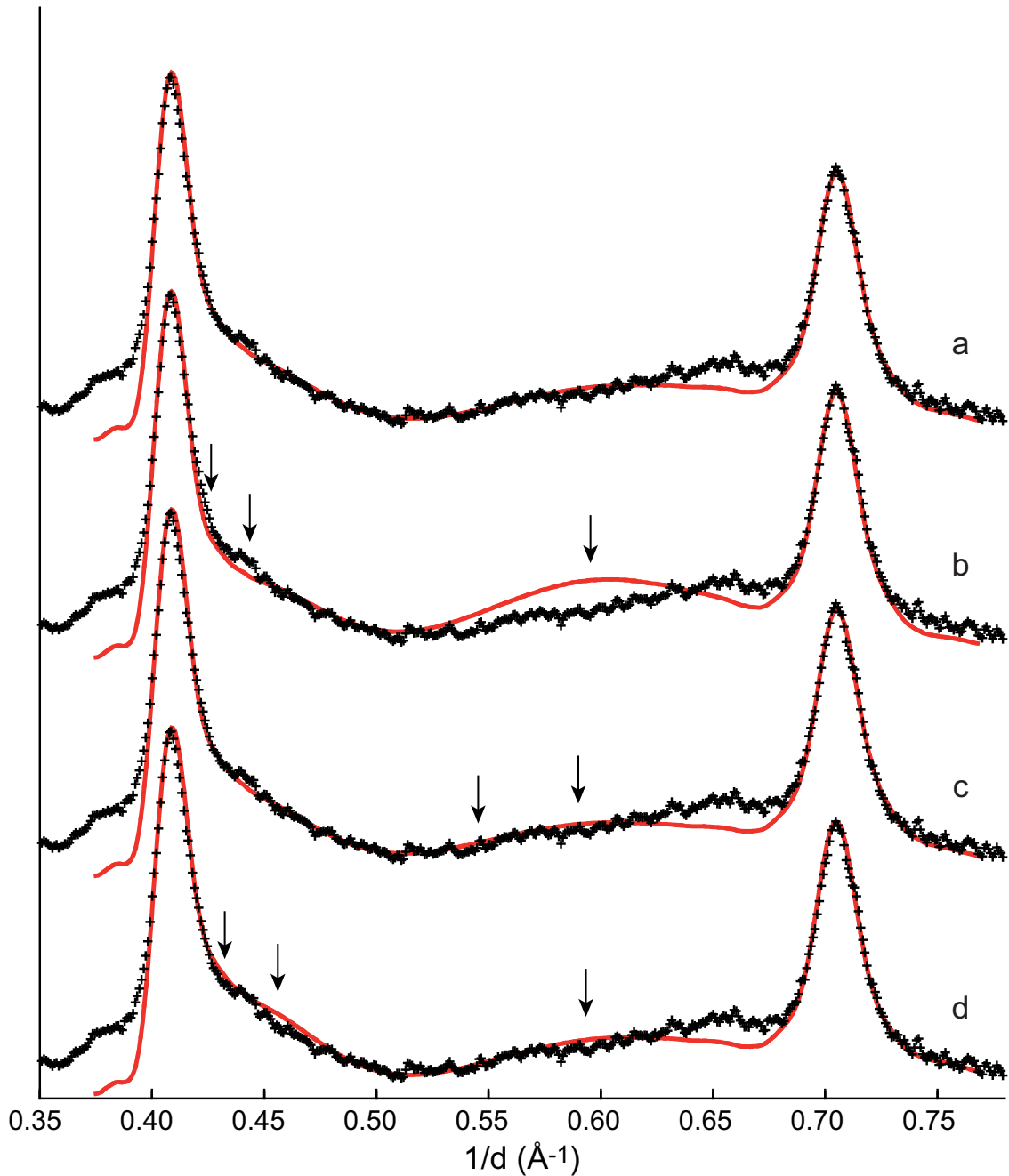


Fig. EA-6: Simulations of the [20,11] and [02,31] X-ray scattering bands (C-centered layer cell, black crosses). Small but significant misfits between experimental and calculated patterns are pointed out with arrows. Intensities (red lines) were calculated with a turbostratic layer stacking (no interlayer correlation). (a) Optimal model (Table 1; Figs. 8 and EA-5); $R_{wp} = 3.49\%$. (b) Model with ^{IV}Zn (Zn2) in (0, 0, 1.97 Å), instead of (0, 0, 1.77 Å) in the optimal fit, so as to increase the Zn-O bond length from 1.82 Å (Table 2) to 1.91 Å. Coordinated H_2O molecules (O4) were moved from (0, 0, 3.70 Å) to (0, 0, 3.90 Å); $R_{wp} = 3.92\%$. (c) Model with ^{VI}Zn (Zn1) in (0, 0, 2.30 Å), instead of (0, 0, 2.20 Å) in the optimal fit so as to decrease the sum valence of Zn1 from 2.3 (Table EA-1) to 2.0. Coordinated H_2O molecules (O2) were moved from (-0.333, 0, 3.45 Å) to (-0.333, 0, 3.65 Å); $R_{wp} = 3.55\%$. (d) Model with Ca in (-0.333, 0, 3.60 Å), instead of (-0.410, 0, 3.60 Å) and equivalent positions in the optimal fit; $R_{wp} = 3.51\%$. Unless specified, all parameters used in calculations are those of the optimal model.

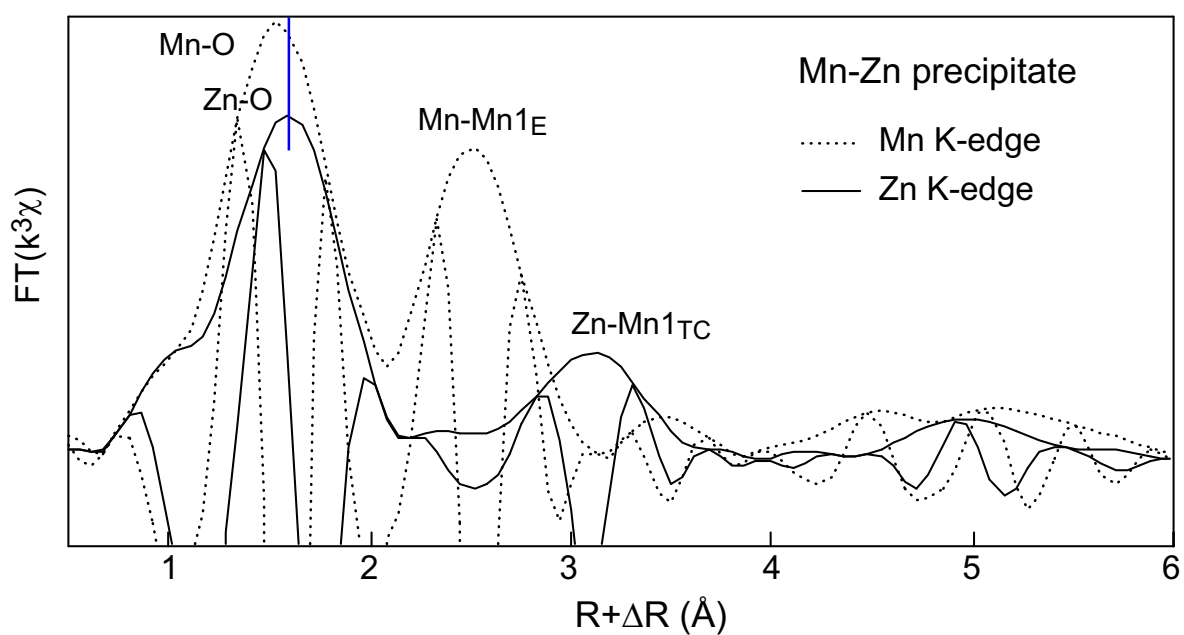


Fig. EA-7: Fourier transform of the EXAFS spectra for the Mn-Zn precipitate at the Mn and Zn K-edges. The average Mn-O and Zn-O EXAFS distances (R values) are 1.90 Å and 2.00 Å, respectively.